Gaillard, N., Williams-Jones, A.E., Clark, J.R., Salvi, S., Perrouty, S., Linnen, R.L., Olivo, G.R., 2020. The use of lithogeochemistry in delineating hydrothermal fluid pathways and vectoring towards gold mineralization in the Malartic district, Québec. Ore Geology Reviews, 120: 103351.

The use of lithogeochemistry in delineating hydrothermal fluid pathways and vectoring towards gold mineralization in the Malartic district, Québec

Authors

Nicolas Gaillard [1], Anthony E. Williams-Jones [1], James R. Clark [1], Stefano Salvi [2], Stéphane Perrouty [3,4], Robert L. Linnen [4], Gema R. Olivo [5]

Affiliations

[1] McGill University, Department of Earth and Planetary Sciences, 3450 University Street, Montréal, QC, H3A 0E8, Canada

[2] Géosciences Environnement Toulouse (GET), Université Paul Sabatier, CNRS, Institut de Recherche pour le Développement, 14 avenue Edouard Belin, F-31400 Toulouse, France

[3] Laurentian University, Mineral Exploration Research Centre, Harquail School of Earth Sciences, Goodman School of Mines, 935 Ramsey Lake Road, Sudbury, ON, P3E 2C6, Canada

[4] Western University, Department of Earth Sciences, 1151 Richmond Street, London, ON, N6A 6B7, Canada

[5] Queen's University, Department of Geological Sciences and Geological Engineering, Kingston, ON, K7L 3N6, Canada

Corresponding author

Nicolas Gaillard
McGill University, Department of Earth and Planetary Sciences
3450 University Street, Montréal, QC, H3A 0E8, Canada
nicolas.gaillard@mail.mcgill.ca

Abstract

The world-class, oxidized intrusion-related Canadian Malartic gold deposit, with reserves estimated at 5.56 Moz Au grading 1.10 g/t Au, and a total geological endowment of 16.3 Moz Au, is one of the largest gold deposits in the Archean Superior Province of Canada. The mineralization is hosted mainly by Pontiac Group metasedimentary rocks, Piché Group metavolcanic rocks, and quartz monzodiorite to granodiorite porphyritic intrusions. The ore takes the form of a low-grade envelope of disseminated pyrite (0.35 to 1 g/t Au) grading inwards into higher grade (>1 g/t Au) stockwork and breccia zones. Hydrothermal alteration in the metasedimentary rocks is zonally distributed around the fluid pathways. Proximal alteration is characterized by a microcline±albite-quartz replacement-type assemblage, with lesser phlogopite, calcite ±Fe-dolomite, pyrite and rutile. The distal alteration assemblage comprises biotite, microcline±albite, phengite, quartz, calcite, pyrite and rutile.

In this study, we assess the magnitude and distribution of fluid-rock interaction in the metasedimentary rocks of the Malartic district. The metaturbidites are separated into four lithotypes based on grain size to reduce the effects of primary depositional processes on mass change calculations. Despite the variability in protolith compositions, the metasedimentary rocks define a geochemically consistent, cogenetic sequence. The results of the mass transfer calculations indicate progressive gains in CO_2-S-K_2O and LOI, as well as Au-Te-W-Ag-(As-Be-Sb-Bi-Mo-Pb), from background, to distal and proximal alteration zones (relative to the least-altered samples). Molar element ratio analysis (alkali/aluminum) indicates an increase in alkali metasomatism (K and Na) adjacent to the main hydrothermal fluid pathways, which is manifested by the progressive stabilization of microcline and albite at the expense of oligoclase, biotite and white mica.

Ore-associated pathfinder elements delineate broad enrichment patterns around the deposit, and are used to understand hydrothermal fluid circulation in the Malartic district. A statistical approach based on a comparison of the results of the mass change calculations with the background composition provides robust constraints on the magnitude and extent of the lithogeochemical haloes. Generally, the alteration forms envelopes that extend along the S_2 fabric, with the largest lithogeochemical anomalies (*e.g.*, Au, W, Te and Ag) reaching up to 10 kilometers in length, and 2 kilometers in width. The results of this study demonstrate that whole-rock lithogeochemistry can provide a valuable tool with which to define vectors toward gold mineralization in a regional exploration context.

Keywords

- Canadian Malartic gold deposit
- Whole-rock lithogeochemistry
- Mass transfer calculations
- Molar element ratio analysis
- Metasomatic haloes
- Exploration vectors

Highlights

- Mass change calculations are used to evaluate the magnitude and spatial distribution of metasomatic processes in the Malartic gold district.
- A statistical method based on Z-score calculations is employed to constrain the magnitude and extent of the lithogeochemical haloes.
- Ore-associated pathfinder elements (*e.g.*, W, Te and Ag) outline broad enrichment patterns that extend several kilometers laterally from the Canadian Malartic deposit.
- Molar element ratio analysis is a reliable method for assessing the mineralogical controls on alkali metasomatism.
- Whole-rock lithogeochemistry provides a valuable tool with which to define vectors toward gold mineralization in a regional exploration context.

1. Introduction

Major gold deposits in metamorphic terranes are typically surrounded by extensive wall-rock alteration haloes manifested by systematic changes in mineralogy away from the hydrothermal fluid pathways (Clark et al., 1989; Eilu and Mikucki, 1998; Bierlein et al., 1998; Eilu et al., 1999; Bierlein et al., 2000; Knight et al., 2000; Eilu and Groves, 2001; Goldfarb et al., 2005). The lateral zonation of alteration reflects the progressive decrease in fluid-rock interaction (*i.e.*, rock-buffering) with increasing distance from the hydrothermal centers (Korzhinskii, 1968; McCuaig et al., 1993; Ridley et al., 1996). Because the variations in alteration mineralogy generally reflect mass transfer, lithogeochemical data can be used to assess the magnitude and spatial distribution of fluid-rock interaction (Bierlein et al., 1998; Eilu et al., 2001; Whitbread and Moore, 2004; Warren et al., 2007; Prendergast, 2007). Methods involving mass balance calculations constitute a quantitative approach to evaluating the effects of metasomatic processes (Gresens, 1967; Grant, 1986; MacLean and Barrett, 1993; Mathieu, 2018). Likewise, molar element ratio analysis can be used to investigate mass transfer processes, and also offers a direct means with which to interpret alteration-related mineralogical reactions (Madeisky and Stanley, 1993; Davies and Whitehead, 1994; Warren et al., 2007). The results of mass transfer calculations and molar element ratio analysis can therefore yield diagnostic parameters for mapping the spatial distribution of alteration defining the footprint of major gold deposits (Eilu and Mikucki, 1998; Eilu et al., 1999; Whitbread and Moore, 2004; Warren et al., 2007; Stock, 2012). Most importantly, ore-related 'pathfinder' elements (*e.g.*, W, Te, Sb, Bi or As) can delineate lithogeochemical anomalies that extend far beyond the limits of the macroscopic hydrothermal alteration (Eilu and Groves, 2001; Whitbread and Moore, 2004; Perrouty et al., 2019).

In this study, we characterize the lithogeochemical signature of hydrothermal alteration at the Canadian Malartic stockwork-disseminated gold deposit (Québec), and extract parameters to map the intensity and distribution of fluid-rock interaction. Mass change calculations are conducted to evaluate the magnitude of the metasomatic transfer and its distribution across the Malartic district. A statistical method based on Z-score calculations is implemented to constrain the spatial extent of the lithogeochemical haloes around the deposit. In addition, molar element ratios are used to assess the mineralogical controls on alkali mobility in the altered metasedimentary rocks. We demonstrate that lithogeochemical data provide a powerful tool with which to outline the regional distribution of alteration features associated with ore-forming processes. This approach offers an efficient means of identifying district-scale alteration footprints around major ore

systems and should prove especially useful in a mineral exploration context by providing potential vectors towards gold mineralization.

2. Regional Geology

The late Archean Abitibi greenstone belt, in the southeast Superior Province, hosts world-renowned gold mining districts such as Val d'Or, Malartic and Rouyn-Noranda (Fig. 1; Robert and Poulsen, 1997; Robert et al., 2005). Many of the major gold deposits occur along a crustal-scale structure, the Cadillac-Larder Lake Fault Zone, which separates the Abitibi greenstone belt to the north from the Pontiac metasedimentary belt to the south (Robert et al., 2005). The former consists of a succession of mafic-ultramafic to felsic volcanic rocks of tholeiitic to calc-alkaline affinity (emplaced from 2750 to 2696 Ma; Ayer et al., 2002), which was succeeded by greywacke-mudstone sedimentation between 2690 and 2685 Ma (Ayer et al., 2005; Frieman et al., 2017). South of the Cadillac-Larder Lake Fault Zone, the Pontiac Group consists of a turbidite sequence dominated by greywacke-mudstone that was deposited from 2685 to 2682 Ma (Davis, 2002). The Timiskaming Group metasedimentary rocks (alluvial-fluvial facies) were deposited unconformably on these older units from 2677 to 2670 Ma (Ayer et al., 2005; Thurston et al., 2008). Several episodes of intrusive magmatism, the onset of which was contemporaneous with early volcanism, continued during and shortly after major tectonic activity (Feng and Kerrich, 1992; Sutcliffe et al., 1993; Davis et al., 2000; Chown et al., 2002). The intrusions range in composition from sodic tonalite-granodiorite (syn-volcanic), through calc-alkaline tonalite and alkaline syenite (syn-tectonic), to S-type two-mica granite and pegmatite (post-tectonic) (see Gaillard et al., 2018 for further detail).

Regional deformation was polyphase, and comprised three main contractional events (Ayer et al., 2002; Perrouty et al., 2017). The first event (D_1) began immediately after the deposition of the turbidite-dominated basins, and consisted primarily of a fold-and-thrust style of deformation (Wilkinson et al., 1999; Bleeker, 2015). The second event (D_2) followed deposition of the Timiskaming-type sedimentary rocks, and was manifested by north-south compression and local strike-slip transpression (Daigneault et al., 2002; Robert et al., 2005). This event was broadly contemporaneous with regional metamorphism (M_2), which ranged in grade from prehnite-pumpellyite to mid-amphibolite facies (Powell et al., 1995). Peak metamorphism was likely reached between 2665 and 2655 Ma, and postdated most of the D_2 deformation (Wilkinson et al., 1999; Ayer et al., 2005; Piette-Lauzière et al., 2019). The third deformational event (D_3) involved dextral transcurrent motion along major fault zones (Daigneault et al., 2002; Ayer et al., 2005).

3. Local Geology

3.1. Lithotypes

The Canadian Malartic deposit is hosted by Pontiac Group metasedimentary rocks, Piché Group metavolcanic rocks, and porphyritic quartz monzodiorite to granodiorite intrusions that postdate these units (Figs. 2-3). The Pontiac Group metasedimentary belt forms a laterally extensive unit that stretches along the Cadillac-Larder Lake Fault Zone (Camiré et al., 1993; Mortensen and Card, 1993). It is composed of greywacke-mudstone successions, the petrographic and lithogeochemical characteristics of which will be described in detail later in this paper (see Sections 6.1 and 6.2). The Piché Group (>2709 Ma; Pilote et al., 2015) forms a thin unit (<2 km across) restricted to the Cadillac-Larder Lake Fault Zone, and consists dominantly of mafic-intermediate to ultramafic metavolcanic rocks, as well as minor mafic to felsic intrusions and metasedimentary rocks (Simard et al., 2013; Bedeaux et al., 2018). In the Malartic district, these units were intruded by a suite of quartz monzodiorite to granodiorite plutons at ~2678 Ma (Helt et al., 2014; De Souza et al., 2016, 2019).

3.2. Deformation and metamorphism

The Malartic district was affected by a complex sequence of deformation (compressional) and metamorphic events (Camiré and Burg, 1993; Benn et al., 1994; Ghassemi, 1996; Perrouty et al., 2017; Gaillard et al., 2018; Piette-Lauzière et al., 2019). The first episode of deformation (D_1) was manifested by isoclinal folding of the Pontiac Group metaturbidites (F_1), and is generally recognized from inversions in the polarity of the sedimentary bedding (Sansfaçon and Hubert, 1990; Perrouty et al., 2017). The second episode of deformation (D_2) produced moderately tight, upright folds (F_2) associated with a penetrative axial-planar cleavage (S_2) (Fig. 4; Sansfaçon, 1986; Trudel and Sauvé, 1992). The S_2 foliation represents the dominant tectono-metamorphic fabric in the district (associated with M_2 metamorphism), and is defined by biotite±white mica and subordinate chlorite, and aligned aggregates of pyrite±pyrrhotite-chalcopyrite (Fig. 4; Gaillard et al., 2018). A third episode of deformation (D_3) is represented by rare chevron folds (F_3) and small-scale kink bands, and is locally associated with chlorite-calcite stringers (Perrouty et al., 2017).

The M_2 metamorphic event in the Malartic district is reflected by a gradual increase in grade from upper greenschist facies (biotite zone) adjacent to the Cadillac-Larder Lake Fault Zone to mid-amphibolite facies (staurolite zone) a few kilometers (1.5 to 2.5 kilometers) to the south (Fig. 2). The axial-planar nature of the

metamorphic foliation (S_2) relative to the F_2 folds suggests that prograde metamorphism (M_2) was broadly coeval with D_2 deformation (Gaillard et al., 2018). In addition, linear inclusion trails oriented parallel to the S_2 foliation in garnet and staurolite are interpreted to reflect a late-kinematic timing for peak metamorphism (M_2) relative to D_2 deformation (Gaillard et al., 2018; Piette-Lauzière et al., 2019). These interpretations are consistent with geochronological evidence from Lu-Hf dating of garnet, which indicates that peak metamorphism occurred at 2657.5±4.4 Ma (Piette-Lauzière et al., 2019).

4. Canadian Malartic Gold Deposit

The Canadian Malartic deposit is a world-class, low grade, large tonnage gold deposit that contains reserves estimated to be 5.56 Moz Au at a grade of 1.10 g/t Au (as of December 31, 2018; Agnico-Eagle annual report). The overall gold endowment of the deposit, calculated from the present and past production, plus mineral reserves and resources (excluding inferred resources) is estimated at 16.3 Moz Au (see Gaillard et al., 2018, and references therein). With an annual production of 0.70 Moz Au in 2018, Canadian Malartic is currently the largest gold mine in Canada.

4.1. Nature and distribution of mineralized zones

Canadian Malartic is a stockwork-disseminated gold deposit consisting of a low-grade (0.35 to 1 g/t Au) semi-continuous halo of pyritic alteration, which generally transitions inwards to higher grade (>1 g/t Au) stockwork and breccia zones (Fig. 3; Robert and Poulsen, 1997). The distribution of the mineralized zones is controlled by three main structures, which are interpreted to have acted as preferential pathways for hydrothermal fluids (Fig. 3). The first of these, the Sladen Fault, is a 3 km-long, W-trending, S-dipping ductile-brittle shear zone, and represents a first-order splay off the Cadillac-Larder Lake Fault Zone (Derry, 1939; Trudel and Sauvé, 1992; De Souza et al., 2015, 2016, 2019). The second structure comprises NW-SE deformation zones, and consists of a series of parallel, high-strain axial-planar to fractured F_2 folds (Sansfaçon and Hubert, 1990; De Souza et al., 2016). The third structure, the Barnat Fault, forms a corridor of anastomosing shears that extend along the southern margin of the Cadillac-Larder Lake Fault Zone, parallel to the NW-SE deformation zones (Trudel and Sauvé, 1992). The gold mineralization also displays a close spatial association with quartz monzodiorite to granodiorite porphyritic intrusions, notably along faulted contacts with the metasedimentary and metavolcanic host rocks (see Fig. 3; Helt et al., 2014; Perrouty et al., 2017; De Souza et al., 2019).

4.2. Hydrothermal alteration

The Canadian Malartic gold deposit consists of stockworks of quartz-biotite-carbonate-microcline± pyrite veinlets (v2) associated with a pervasive microcline-albite-biotite±(phengite)-carbonate-pyrite alteration (Robert, 2001; De Souza et al., 2016; Gaillard et al., 2018). Systematic variations in alteration reflect a lateral zonation of hydrothermal activity away from the fluid corridors (De Souza et al., 2016, 2019; Gaillard et al., 2018). The proximal alteration is manifested by a beige-brown replacement-type assemblage dominated by microcline±albite-quartz, with variable proportions of phlogopite, calcite, Fe-dolomite, pyrite and rutile (Fig. 5A-B). This alteration displays a strong genetic association with ore-stage (v2) veinlets, and coincides spatially with a high density of veins in stockwork and breccia zones (Fig. 5A-B).

In the metasedimentary rocks, the proximal alteration transitions outwards to a blue-grey distal alteration assemblage consisting of biotite, microcline±albite, phengite, quartz, calcite, pyrite and rutile (Fig. 5C-D). The intensity of the distal alteration was controlled mainly by ore-stage (v2) veinlets, as manifested by a broad correlation of pyrite and calcite alteration with vein (v2) density. The transition from proximal to distal alteration is accompanied by a gradual increase in the proportions of biotite (Mg-rich) and white mica (phengite) at the expense of microcline±albite (Fig. 5C-D). The mineralogy of the distal assemblage was affected by the composition of the metasedimentary rocks, as indicated by increased phengite alteration in fine-grained mudstone beds (De Souza et al., 2016; Gaillard et al., 2018; Lypaczewski et al., 2019) (Fig. 5C).

In addition, hydrothermal alteration is also manifested by a broad sulfidation-oxidation halo surrounding the main fluid pathways (Gaillard et al., 2018). This halo is delineated by systematic outward transitions in Fe-sulfide (from pyrite to pyrite±pyrrhotite) and Fe-Ti oxide (from rutile to ilmenite) minerals, and typically extends a few meters beyond the limit of the ore-shell (>0.35 g/t Au). These transitions are interpreted to reflect decreases in sulfidation ($\sum a$S) and oxidation (fO_2) away from the hydrothermal corridors (Nesbitt, 1986*a*,*b*; Neumayr et al., 2008; Gaillard et al., 2018). Likewise, the transition from proximal calcite±Fe-dolomite to distal calcite-only is interpreted to have resulted from a decrease in $X(CO_2)$ away from the main fluid pathways (Clark et al., 1989).

4.3. Ore mineralogy

Gold mineralization at Canadian Malartic consists of native gold and Au-(Ag)-bearing telluride minerals in quartz-biotite-carbonate-microcline±pyrite (v2) veinlets and associated alteration envelopes (Helt et al.,

2014; De Souza et al., 2016; Gaillard et al., 2018). The ore assemblage consists of native gold, petzite (Ag_3AuTe_2) and calaverite ($AuTe_2$), together with hessite (Ag_2Te), altaite (PbTe) and minor Bi-bearing tellurides (Helt et al., 2014). These minerals are generally accompanied by minor chalcopyrite and galena, as well as rare sphalerite and molybdenite. Mineralogical and textural observations indicate a consistent association of native gold and telluride minerals with disseminated pyrite (Helt et al., 2014; Gaillard et al., in review). This association is generally manifested by gold-bearing minerals in the vicinity of, or in direct contact with pyrite grains. Native gold and Au-(Ag)-telluride minerals also occur as small (sub-micron) inclusions and nano-particles in the pyrite, as indicated by elevated Au and ore-related element (Ag, Te, Pb and Bi) concentrations (Gao et al., 2015; Gaillard et al., in review). Hydrothermal pyrite displays composite textures manifested by three paragenetic stages (Type 1 to 3), in the first and second of which the pyrite is interpreted to have precipitated from ore-forming fluids (Gaillard et al., in review).

4.4. Deposit classification

Early studies of the Canadian Malartic deposit placed it in the porphyry (Issigonis, 1980) and orogenic classes of deposits (Trudel and Sauvé, 1992) and a subsequent study by Robert (2001) classified it as a syenite-associated stockwork-disseminated gold deposit. Recently, based on a spatial association of the gold mineralization with quartz monzodiorite to granodiorite intrusions (Fig. 3) and the oxidized nature of the ore-forming fluid, Canadian Malartic has been classified as an oxidized intrusion-related gold deposit (Helt et al., 2014). Finally, De Souza et al. (2016) reported evidence of two separate stages of ore formation, an early magmatic-hydrothermal stage and a later syn-D2 deformation stage that might have involved remobilization of the early gold mineralization. They did not, however, attempt to classify the deposit.

4.5. Sampling strategy

A total of 596 metasedimentary rock samples were collected and analyzed for whole-rock major and trace element compositions (see Piercey et al., 2014, for details of the sampling protocol); sampling was restricted to the Pontiac Group rocks to facilitate the evaluation of fluid-rock interaction. The drill core and surface samples were taken from homogeneous intervals representative of the lithology and hydrothermal alteration at each site. Sampling was distributed across the Malartic district over an area of approximately 15×7.5 kilometers, thereby providing a regional framework in which to assess the metasomatic effects associated with fluid-rock interaction (Fig. 2). Sampling density was increased near, and in the deposit to

elucidate the lithogeochemical signatures of the proximal and distal alteration facies. The regional distribution of samples was designed to characterize the background geochemical variations of the Pontiac Group metasedimentary rocks. With respect to the latter, samples were divided into three groups according to their alteration characteristics, from background (n=443) with no visible evidence of hydrothermal alteration, to distal (n=123) and proximal (n=30) alteration types.

4.6. Whole-rock lithogeochemical analyses

The samples were crushed, split and pulverized with mild steel to <75 µm (package Prep-31) by ALS Canada (Vancouver, BC). The major and minor element compositions were determined after lithium fusion using wavelength dispersive X-ray fluorescence analysis (package 4C-XRF Fusion) by Activation Laboratories (Ancaster, ON). The minor and trace element compositions, including those of the rare earth elements (REE), were analyzed using a combination of ICP-AES and -MS after sodium peroxide fusion (package GE ICM90A) by SGS Canada (Burnaby, BC). Whole-rock major, minor and trace element compositions, including gold concentrations, were also determined using ICP-AES and ICP-MS analysis following partial digestion with aqua regia (package ME-MS41L) by ALS Canada. Whole-rock sulfur and carbon analyses were carried out using a LECO analyzer (IR absorption spectroscopy after combustion) by SGS Canada (package GE CSA06V). The accuracy and precision of the whole-rock lithogeochemical analyses were monitored through incorporation of standard, blank and duplicate samples. Details of the quality control and assurance protocols (QA/QC), and cross-validation results are provided in Perrouty et al. (2019). The complete lithogeochemical dataset (raw analyses) is reported in Appendix 1.

4.7. Evaluation and preparation of the lithogeochemical dataset

A systematic approach was implemented to evaluate the lithogeochemical dataset as a prerequisite for further investigation and statistical analysis. Elements with more than 5% of values below the lower detection limit (non-detects) were discarded (left-censored datasets). In addition, elements with a large number of values close to the detection limit (*i.e.*, more than 50% of analyses below 3×LOD value) were also removed. The presence of non-detect values is typically a source of complication for subsequent data analysis and calculation of summary statistics (Helsel, 2005; Huston and Juarez-Colunga, 2009). Simple methods for handling censored values (deletion or arbitrary replacement) typically disregard the effects of closure that characterize compositional data (Aitchison, 1986) and have been shown to generate biased estimates of the mean and variance (Helsel and Gilliom, 1986; Makvandi et al., 2016). In this

study, a multivariate imputation method was implemented to replace the censored values using the `zCompositions` package in the R software environment (Hron et al., 2010; Palarea-Albaladejo and Martin-Fernández, 2015). This method relies on the robust isometric log-ratio expectation-maximization algorithm, an iterative compositional procedure that estimates the non-detects through the preservation of the relative covariation structure of the dataset (Palarea-Albaladejo et al., 2014).

4.8. Mass change calculations

Mass transfer associated with hydrothermal alteration was calculated following the principles of Gresens (1967), wherein the evaluation of mass changes is based on a comparison of altered rock compositions to those of their least-altered rock equivalents (precursors). In the absence of density measurements, the overall mass/volume change caused by hydrothermal alteration was estimated using immobile element ratios (MacLean, 1990). Elements such as Al, Ti and Zr are generally considered to be immobile in hydrothermal systems under a wide range of physico-chemical conditions (Finlow-Bates and Stumpfl, 1981; MacLean and Barrett, 1993). Because immobile element pairs maintain constant ratios during alteration, the selection of immobile elements for mass change calculations can be assessed graphically from their linear relationships in bi-variate plots (MacLean and Kranidiotis, 1987). As shown by Warren et al. (2007), the use of immobile element ratios in place of density and volume factor terms yields a simplified expression of the Gresens' mass change equation, which is equivalent to that of MacLean and Barrett (1993). This approach involves the calculation of the reconstructed composition of a component X, corrected for the overall mass/volume change produced by hydrothermal alteration:

$$RC^{A}_{X} = C^{A}_{X} \times (C^{P}_{imm.} / C^{A}_{imm.}) \quad (1)$$

where:

- RC^{A}_{X} is the reconstructed composition of a component X in sample A (altered rock)
- C^{A}_{X} is the concentration of a component X in A (altered rock)
- $C^{P}_{imm.} / C^{A}_{imm.}$ is the concentration ratio of an immobile component in P (precursor) to A (altered rock)

In this study, the mass changes are expressed relative to the composition of the precursor rock, and correspond to the ratio of the reconstructed composition of a component X in the sample of interest to the concentration of the same component in the precursor rock:

$$\Delta_X = RC^A_X / C^P_X \quad (2)$$

where:

- Δ_X is the mass change (concentration factor) of a component X, relative to the precursor composition
- C^P_X is the concentration of a component X in P (precursor)

The expression of the mass transfer as a ratio relative to the precursor composition (concentration factor) yields results that are restricted to the positive number space, and facilitates data manipulation for subsequent statistical calculations (*e.g.*, log-transformation) and map representation (see Perrouty et al., 2019). In this context, values below unity indicate depletions, whereas values above unity represent enrichments relative to the least-altered samples. A compilation of the mass transfer data is provided in Appendix 2.

4.9. Lithogeochemical mapping and spatial data analysis

The results of the mass change calculations are presented as a series of maps that illustrate the regional distribution of fluid-rock metasomatic interactions in the metasedimentary rocks of the Malartic district. The dataset used to produce the lithogeochemical maps is reported separately in the supplementary material attached to this study (Appendix 3).

Because the criteria selected for the spatial representation of the mass changes remain partly arbitrary (*e.g.*, the color scale), a statistical approach was implemented to investigate the magnitude and distribution of the metasomatic haloes. The aim of this method is to establish a statistical framework in order to compare the spatial extent of the different lithogeochemical anomalies, and thus provide robust constraints on the mobility of the pathfinder elements. Our approach therefore consists of formulating the mass balance results in terms of standard deviation distance relative to the background population mean (standard score). This method is generally referred to as standardization and is most commonly applied to normally-distributed datasets. For most elements, however, the distribution of the mass change data in the background metasedimentary rock population (n=443) is best approximated by a log-normal distribution. For this reason, the geometric mean ($\bar{x}^*$) and multiplicative standard deviation (s^*) were used to characterize the central tendency and dispersion of the data, respectively (Limpert et al., 2001). Given a component X, these parameters are expressed as:

$$\bar{x}^* = \exp\left(\frac{1}{n} \cdot \sum_{i=1}^{n} \ln(x_i)\right) \quad (3)$$

$$s^* = \exp\left(\sqrt{\frac{1}{n-1} \cdot \sum_{i=1}^{n} \left[\ln\left(\frac{x_i}{\bar{x}^*}\right)\right]^2}\right) \quad (4)$$

where:

- n represents the number of observations
- x_i corresponds to the mass change values (Δ_X) calculated for a component X

Accordingly, the geochemical anomalies are evaluated relative to the background compositions using a standardization algorithm that is based upon the multiplicative properties of the log-normal distribution:

$$Z^*_{\Delta X} = \frac{\ln(x_i) - \ln(\bar{x}^*_{background})}{\ln(s^*_{background})} \quad (5)$$

where:

- $Z^*_{\Delta X}$ is the standardized mass change value for a component X relative to the background distribution
- x_i is the mass change value (Δ_X) calculated for a component X
- $\bar{x}^*_{background}$ represents the geometric mean of the background population
- $s^*_{background}$ represents the multiplicative standard deviation of the background population

Interpolated maps of the mass change data (standardized values; *i.e.*, $Z^*_{\Delta X}$) were produced using a minimum curvature gridding algorithm in the Geosoft Oasis Montaj software. A unique color scale based on multiples of the standard deviation distance to the mean value (log-transformed) was used for all the variables (class interval representation).

5. Pontiac Group Metasedimentary Host Rocks

5.1. Petrography of the background metasedimentary rocks

The Pontiac Group metasedimentary rocks form a flyschoid sequence composed of interstratified beds of mudstone (pelitic) to greywacke (psammitic) (Dimroth et al., 1982; Mortensen and Card, 1993; Ghassemi, 1996). The planar-stratified sedimentary beds range in thickness from a few centimeters up to a meter, and generally display parallel, millimeter-scale internal laminations (Fig. 4A-B). Individual strata commonly show evidence of graded-bedding, as manifested by a progressive upward decrease in detrital

grain size (Fig. 4A-B). The clastic particles range in diameter from <50 µm in mudstone, to 2 mm in greywacke, and reach a maximum of 12 mm in rare conglomeratic beds (Ghassemi, 1996). The vertical succession of the sedimentary facies is generally consistent with a partial Bouma sequence, which suggests that the Pontiac Group wackes were deposited from turbidity currents (Benn et al., 1994; Card and Poulsen, 1998). This interpretation is supported by the presence of internal sedimentary structures typical of turbidites, including load casts, cross-laminations and flame structures (Ricci-Lucchi and Amorosi, 1978; Goulet, 1978).

The mineralogy of the Pontiac Group metasedimentary rocks varies systematically as a function of the protolith grain size and metamorphic grade. The greenschist facies metaturbidites are composed of quartz, plagioclase (oligoclase) and biotite, with lesser but variable proportions of white mica, chlorite, epidote, ilmenite, pyrite, pyrrhotite and magnetite (Fig. 4C-E). Because finer-grained turbidite layers originally contained a greater proportion of clay minerals, the mudstone facies generally displays higher modal proportions of white mica and biotite than the greywacke. Such modal variations are interpreted to reflect changes in bulk-rock composition caused by primary sedimentary processes (*e.g.*, the aluminous nature of pelitic layers). At higher metamorphic grade, variations in protolith composition partly determined the mineralogy of the peak metamorphic assemblage; more specifically, staurolite (and garnet) porphyroblasts formed preferentially in the fine-grained pelitic beds of the turbiditic sequence (see Gaillard et al., 2018; Piette-Lauzière et al., 2019). The metamorphic index minerals provide key indicators for discriminating among the sedimentary facies at higher metamorphic grade (*i.e.*, amphibolite facies), wherein metamorphic recrystallization of quartz and plagioclase typically forms a granoblastic polygonal texture that obliterates the primary sedimentary textures (Ghassemi, 1996).

5.2. Lithogeochemistry of the background metasedimentary rocks

The variations in protolith grain size are manifested by consistent changes in bulk-rock lithogeochemical compositions. Such variations are interpreted to mainly reflect the effects of physical sorting (grain size and density) during transport and deposition of the clastic sediments (Fig. 4). The metasedimentary rocks were therefore separated into four lithotypes based on textural (grain size) and mineralogical characteristics in order to evaluate the effects of sedimentary processes on lithogeochemical variability (Cai et al., 2008; Mishra and Sen, 2011). These lithotypes are greywacke (n=247), siltstone (n=134) and mudstone (n=188), as well as a group defined by lower ∑REE concentrations and a distinct chondrite-normalized REE profile

348 (n=27). The variations in whole-rock major element concentrations among the lithotypes in the background
349 (non-altered) metasedimentary rocks are illustrated in Figure 6 using box and whisker diagrams (additional
350 plots for minor and trace elements are provided in Appendix 4).

351 The greywacke (coarse-grained) fraction of the metasedimentary rocks is generally characterized by
352 higher concentrations of SiO_2 (average 66.1 wt.% in the background population) relative to the siltstone
353 (65.0 wt%) and mudstone (60.9 wt%) fractions (Fig. 6). In addition, the greywacke also has elevated
354 concentrations of Na_2O (3.73 wt%) and CaO (2.59 wt%) compared to the siltstone (3.64 and 2.48 wt%,
355 respectively) and mudstone (2.96 and 2.10 wt%, respectively) (Fig. 6). These variations are interpreted to
356 reflect higher modal proportions of quartz and plagioclase in the coarse-grained sediments (Fig. 4). In
357 contrast, the mudstone (fine-grained) fraction has higher average concentrations of Al_2O_3 (17.7 wt%)
358 relative to siltstone (15.7 wt%) and greywacke (15.3 wt%). In addition, increases in the concentrations of
359 Fe_2O_3 (from 5.32 to 6.66 wt%), K_2O (from 2.09 to 3.27 wt%), MgO (from 2.77 to 3.45 wt%) and TiO_2
360 (from 0.54 to 0.67 wt%) from greywacke to mudstone are also associated with decreasing grain size (Fig. 6).
361 These trends are interpreted to be due mainly to higher proportions of hydrous phyllosilicates (dominantly
362 biotite and white mica) in the fine-grained fractions of the sediment, and likely correspond to elevated
363 proportions of clays in the protolith (Fig. 4; Camiré et al., 1993). This interpretation is supported by an
364 increase in loss on ignition (LOI), from 1.25 wt% in the greywacke, to 1.98 wt% in the mudstone (Fig. 6).
365 These trends also coincide with a progressive increase in the average concentrations of most minor elements
366 (*e.g.*, Ba, Cr, V, Rb, Ni, Co, Ga) with decreasing grain size. The exceptions are decreasing trends in Sr and
367 Zr concentration (Appendix 4). The minor element enrichments documented for the fine-grained fractions
368 are interpreted to be due to greater proportions of phyllosilicates (biotite±white mica) and subordinate
369 oxides (ilmenite±magnetite), whereas the opposing trends (*i.e.*, towards the greywacke fraction) are likely
370 due to dilution by quartz and plagioclase (Cai et al., 2008; Mishra and Sen, 2011). The low ∑REE group
371 of metasedimentary rocks has major (Fig. 6) and minor (Appendix 4) element compositions that are
372 intermediate between those of siltstone and mudstone. However, the low ∑REE sediments are consistently
373 depleted in REE (Fig. 7) and have lower proportions of Ni and Co compared to the other lithotypes
374 (Appendix 4).

375 Despite the variability in protolith compositions as a result of primary sedimentary processes, the linear
376 variations documented for the Pontiac Group metaturbidites on immobile-immobile bi-variate diagrams

point to a lithogeochemically uniform metasedimentary sequence (Helt et al., 2014). The positive correlation between Al_2O_3 and TiO_2 (r=0.78) suggests a strong cogenetic relationship across the stratigraphic sequence (Fig. 7A). The geochemical signatures of the metaturbidites were also assessed by comparing REE profiles normalized to chondrite composition (Fig. 7B). Aside from a limited number of samples characterized by a distinct signature and a low total ∑REE content (n=27), the resulting profiles are nearly identical and differ mainly in the absolute REE concentrations (n=569). These similarities suggest that the Pontiac Group metaturbidites likely had a single provenance (Camiré et al., 1993), although the low ∑REE population may reflect an intermittent (and minor) contribution of clastic material from another source (Fig. 7B).

6. Mass Transfer in Hydrothermally Altered Metasedimentary Rocks

The mass changes associated with hydrothermal alteration in the metasedimentary rocks define the lithogeochemical signature of the Canadian Malartic deposit, and can be used to develop parameters for mapping the intensity and distribution of fluid-rock interaction at the district scale. However, as noted above, evaluation of mass transfer in the sedimentary rocks is commonly hampered by geochemical variability in protolith compositions (Fig. 6; Appendix 4). To reduce the effect of such variations, the mass transfer calculations were conducted separately for each of the main lithotypes. Because the background populations of the greywacke, siltstone, mudstone and low ∑REE sediments display relatively narrow compositional ranges, the primary variations in each lithotype are interpreted to be negligible compared with those of the sedimentary sequence as a whole, thereby providing an appropriate rock classification to quantify mass transfer associated with hydrothermal alteration (Fig. 6; Appendix 4).

6.1. Least-altered samples

A set of least-altered samples (n=20) was selected from the Pontiac Group metasedimentary host rocks based on petrographic (textural and mineralogical features) and lithogeochemical characteristics. Average least-altered compositions were calculated separately for each of the lithotypes from representative samples of greywacke (n=6), siltstone (n=4), mudstone (n=6), and low ∑REE (n=4) metasedimentary rocks. The least-altered samples were carefully inspected to avoid effects of hydrothermal alteration or surficial weathering. Because gold mineralization is typically associated with disseminated pyrite and carbonate (calcite±Fe-dolomite) alteration, the criteria for the selection of the least-altered samples included low concentrations of Au (<5 ppb), S (<0.3 wt%) and C (<0.3 wt%). The distance to the ore shell was also taken

406 into consideration, so that the least-altered samples were derived from drill core and outcrops located >1.5
407 kilometers from the Canadian Malartic deposit.

408 ### *6.2. Immobile elements*

409 The overall effects of mass/volume changes caused by hydrothermal alteration were evaluated by
410 normalizing the compositions of the altered samples to those of their respective least-altered precursors
411 using immobile element ratios (MacLean and Kranidiotis, 1987). Element immobility was tested using
412 bi-variate plots, in which immobile elements define linear arrays through the origin (MacLean, 1990). The
413 bulk-rock concentrations of Al_2O_3 and TiO_2 were shown to delineate the best linear trend (r=0.78; Fig. 7A),
414 thereby suggesting that these elements remained immobile during alteration (MacLean and Barrett, 1993;
415 Helt et al., 2014; De Souza et al., 2019). Immobile element ratios calculated from Al_2O_3 concentrations
416 were therefore used to assess the mass changes associated with hydrothermal alteration.

417 ### *6.3. Mass changes associated with hydrothermal alteration*

418 Average mass changes were determined for proximal and distal alteration assemblages to evaluate the
419 metasomatic effects associated with ore-forming processes, and to identify potential pathfinder elements
420 that could be used as vectors to gold mineralization. The results are presented as a series of box and whisker
421 diagrams in Figures 8 and 9 for the distal (n=123) and proximal (n=30) alteration zones, and are evaluated
422 relative to the background metasedimentary rock population (n=443) (Appendix 2). Comparison of the
423 average compositions of the altered and least-altered rocks (n=20) indicates a significant increase in the
424 concentrations of Au-Te-W-Ag-(As-Be-Sb-Bi-Mo-Pb) as well as CO_2-S-K_2O-LOI in the rocks associated
425 with gold mineralization (Figs. 8-9).

426 The results of mass transfer calculations identify systematic enrichments from background, to distal and
427 proximal alteration zones. The proximal and distal alteration assemblages are characterized by substantial
428 gains in C (mean Δ_{CO2} = 56.2 and 21.0, respectively), S (Δ_S = 18.4 and 4.8), K (Δ_{K2O} = 2.6 and 1.7) and
429 LOI (Δ_{LOI} = 6.3 and 3.0), compared to least-altered equivalents (Fig. 8). These observations are consistent
430 with mineralogical characteristics of the alteration assemblages, and correlate with increasing modal pro-
431 portions of calcite±Fe-dolomite and pyrite with increasing proximity to the hydrothermal fluid pathways
432 (De Souza et al., 2016, 2019; Gaillard et al., 2018). Potassium addition in hydrothermally-altered rocks is
433 interpreted to reflect the effects of microcline and biotite±white mica alteration (Fig. 5; Helt et al., 2014;
434 Gaillard et al., 2018; De Souza et al., 2019). Small, but significant gains in Na (Δ_{Na2O} = 1.37 and 1.06

435 in proximal and distal alteration zones, respectively) and Ca (Δ_{CaO} = 1.48 and 1.13) are restricted mainly
436 to the proximal alteration assemblage, and are associated with pervasive feldspathic (microcline±albite)
437 and carbonate alteration (Fig. 8). Other major elements, including Si (Δ_{SiO2} = 0.99 in altered rocks), Mg
438 (Δ_{MgO} = 1.06), Ti (Δ_{TiO2} = 1.09) and Fe (Δ_{Fe2O3} = 1.11) display limited mass changes related to fluid-rock
439 interaction, and their proportions are relatively constant in the different alteration zones (Appendix 2).

440 Gold mineralization in the proximal and distal alteration zones is associated with major gains in Au
441 (Δ_{Au} of 1968 and 586, respectively), as well as substantial enrichments in Te (Δ_{Te} of 146.2 and 21.5),
442 W (Δ_{W} of 65.8 and 17.1), Ag (Δ_{Ag} of 41.7 and 6.8), As (Δ_{As} of 16.8 and 13.8), Be (Δ_{Be} of 8.4 and 3.8),
443 Sb (Δ_{Sb} of 5.3 and 3.3), Bi (Δ_{Bi} of 7.4 and 2.3), Mo (Δ_{Mo} of 13.8 and 2.2) and Pb (Δ_{Pb} of 6.3 and 2.5)
444 relative to least-altered equivalents (Fig. 9). These enrichments are consistent with the mineralogy of the
445 ore assemblage, and thus define the metallic signature of the deposit (Helt et al., 2014; Gaillard et al., 2015;
446 De Souza et al., 2019). Substantial mass gains documented for Au, Te, Ag, Pb and Bi in the mineralized
447 samples reflect the presence of native gold and Au-Ag-(Pb-Bi)-bearing telluride minerals such as petzite,
448 hessite, altaite and calaverite (Gaillard et al., in review). By contrast, bulk enrichments in W and Sb in the
449 altered rocks are attributed to rutile, which has been shown at Canadian Malartic to have anomalously high
450 contents of these elements (J. Clark, pers. comm., 2018).

451 ### *6.4. Inter-element mass change correlations*

452 The mineralogical controls on the metasomatic processes associated with ore formation were evaluated
453 from correlations among the mass change values for the different elements (Fig. 10). Given the relative
454 nature of the mass transfer calculations (*i.e.*, normalization to a precursor composition), such correlations
455 do not suffer the effects of closure that generally affect compositional data (Aitchison, 1986). In addition,
456 these correlations are less influenced by primary depositional features compared to raw lithogeochemical
457 data, and thus provide insights into the mechanisms that govern metasomatic reactions and metal
458 distribution (Libbey and Williams-Jones, 2016).

459 The linear correlation (r=0.66) between Δ_{Au} and Δ_{S} mass changes reflects a close spatial and genetic
460 relationship between gold mineralization and sulfide minerals (Fig. 10). Gold mass change values (Δ_{Au})
461 also correlate positively with Δ_{Te} (0.66) and Δ_{Ag} (0.62), suggesting similar modes of transport and
462 precipitation for Au, Ag and Te (Fig. 10). These interpretations are supported by petrographic observations,
463 most notably the association of native gold and (Au±Ag)-telluride minerals in inclusions and filling

fractures in hydrothermal pyrite (Gaillard et al., in review). For these reasons, gold deposition has been interpreted to have resulted from the destabilization of gold-bisulfide complexes in response to wall-rock sulfidation (Helt et al., 2014). In addition, gold mass change values correlate positively with those of other associated metals, including Δ_W (0.66), Δ_{Be} (0.58) and Δ_{Bi} (0.48) (Fig. 10). Because the enrichment factors calculated for these trace elements are log-normally distributed, the correlations are best characterized by log-transformed values (Appendix 5). Most significantly, the correlations among log-transformed values demonstrate a strong association of Δ_{Au} with Δ_{Ag} (0.82), Δ_{Te} (0.80), Δ_W (0.78), Δ_{Be} (0.70), Δ_{As} (0.54), Δ_{Bi} (0.53) and Δ_{Pb} (0.50). These results compare well with element correlation values calculated by Helt et al. (2014) and De Souza et al. (2019) using the raw lithogeochemical data. Consequently, as discussed below, these metals can be used as pathfinder elements for identifying areas affected by alteration, and in vectoring toward ore zones in the Malartic district (see Eilu and Mikucki, 1998).

Because major element data reflect the primary rock-forming minerals in the host metasedimentary rocks, mass transfer associated with hydrothermal alteration for these components typically results in smaller mass changes than for the trace elements. For this reason, the correlation coefficients for major element mass changes are generally lower than those of the pathfinder metals (Fig. 10). Nonetheless, major element mass changes directly reflect the effects of fluid-rock interaction on alteration mineralogy, and thus provide important information with which to evaluate the magnitude of metasomatic reactions adjacent to hydrothermal fluid pathways (Eilu and Groves, 2001; Whitbread and Moore, 2004). The data presented above indicate a strong colinear relationship between Δ_{LOI} and Δ_{CO2} mass changes (r=0.84), as well as weaker positive correlations between Δ_{CaO} and Δ_{CO2} (r=0.51) and Δ_{CaO} and Δ_{LOI} (r=0.40); these are interpreted to reflect carbonate alteration (Fig. 10). High correlation coefficients between Δ_{LOI} and Δ_S (r=0.75), and between Δ_{CO2} and Δ_S (r=0.64) further indicate a strong coupling of sulfide (pyrite) and carbonate (calcite±Fe-dolomite) alteration. Host-rock sulfidation was also accompanied by pervasive alkali metasomatism (K_2O and Na_2O), as demonstrated by a strong positive correlation relationship between $\Delta_{K2O+Na2O}$ and Δ_S mass changes (r=0.72). The above notwithstanding, Δ_{K2O} displays a weak negative correlation with Δ_{Na2O} (r=-0.29), which suggests complex mineralogical and physico-chemical controls on potassic-sodic alteration in zones of pervasive microcline±albite replacement (Mathieu, 2018; see below).

7. Molar Element Ratios

The mineralogical reactions that controlled mass transfer during hydrothermal fluid-rock interaction were evaluated using molar element ratios (Madeisky and Stanley, 1993; Whitbread and Moore, 2004; Prendergast, 2007; Stanley, 2017). This approach is particularly well-suited to the analysis of metasomatic processes, as molar proportions provide a direct means of correlating changes in bulk-rock composition to alteration mineralogy (Madeisky and Stanley, 1993; Warren et al., 2007). Because they are expressed relative to a conserved component, Pearce element ratios are not affected by closure, and can be used to quantify the lithogeochemical and mineralogical variations associated with hydrothermal alteration (Pearce, 1968; Madeisky and Stanley, 1993). Binary plots based on alkali/aluminum molar ratios (Na/Al *vs*. K/Al) are shown in Figure 11, and illustrate the mineralogical controls on alkali mobility in the metasedimentary rocks of the Malartic district (Davies and Whitehead, 1994, 2006). Specific nodes in such binary plots represent stoichiometric proportions of common alteration minerals, including feldspars (microcline, albite and oligoclase) and phyllosilicates (biotite, white mica and chlorite) (Fig. 11; Warren et al., 2007). However, molar element ratio binary plots only capture a partial representation of the complexity of the system, thereby limiting the evaluation of mass transfer processes to the projected mineral phases.

Two versions of the same molar element ratio binary plot (Na/Al *vs*. K/Al) are presented in Figure 11. In the first, the metasedimentary rocks are color-coded based on petrographic characteristics (grain size) to illustrate the effects of depositional processes on whole-rock composition (Fig. 11A). Most background metasedimentary rocks at Malartic fall within the field outlined by the minerals typical of the metamorphic assemblage, namely biotite, white mica and oligoclase (Fig. 11A). Increasing grain size from mudstone to greywacke is accompanied by a general trend toward higher Na/Al and lower K/Al values (Fig. 11A). These variations are interpreted to reflect progressive mineralogical changes with increasing grain size, as shown by a trend toward the plagioclase (oligoclase) stoichiometric node (*i.e.*, away from biotite and white mica) (Fig. 11A; Davies and Whitehead, 1994; 2006). These results suggest that variations in protolith composition caused by sedimentary processes exerted a strong control on the mineralogy of the background metamorphic assemblage.

Metasomatic effects associated with ore-forming processes were evaluated by dividing metasedimentary rocks according to their hydrothermal alteration characteristics (Fig. 11B). Mass transfer in the altered rocks is manifested by a general increase in K/Al and/or Na/Al ratios relative to background composition, in good

agreement with the results of De Souza et al. (2019). These variations correspond to a broad gradient from background through distal to proximal alteration facies, which is interpreted to reflect progressive changes in mineralogy (and mineral chemistry) in response to increasing alteration intensity (*i.e.*, increase in fluid-rock interaction). The metasedimentary rocks that underwent distal alteration mostly fall within a field delimited by biotite, white mica and albite, and partially overlap the compositions of the background samples (Fig. 11B). By contrast, the metasedimentary rocks from the proximal alteration zone are characterized by elevated K/Al ratios, and fall within a narrow compositional field bounded by biotite, microcline and albite. These results, together with petrographic observations, suggest that increasing alkali (K and Na) metasomatism from distal to proximal alteration zones was due to the increasing stability of microcline and albite, at the expense of oligoclase, biotite and white mica. Molar element ratios therefore provide a powerful means with which to evaluate the distribution of alteration minerals in the footprint of major hydrothermal systems.

8. Spatial Distribution of Hydrothermal Fluid-Rock Interaction

The results of the mass transfer calculations were used to assess the magnitude and spatial distribution of metasomatic processes in the metasedimentary rocks of the Malartic district. A set of geochemical maps is presented in Figure 12 to illustrate the distribution of mass changes for selected major (alkali and volatile) and pathfinder elements. For this purpose, the mass transfer data for each component (Appendix 2) were first transformed using a Z-score standardization algorithm ($Z^{*}_{\Delta X}$), and expressed in units of multiplicative standard deviation (s^{*}) relative to the geometric mean ($\bar{x}^{*}$) of the background distribution (see Section 5.5; Appendix 3). This approach enables direct comparison of the metasomatic haloes (spatial extent and magnitude).

The spatial distribution of the gold mass changes (Δ_{Au}) delineates a broad envelope of elevated values centered on the Canadian Malartic deposit (Fig. 12A). As expected, the strongest gold enrichment is in the deposit area, and generally corresponds to values exceeding the average background composition by more than two multiplicative standard deviations (*i.e.*, $Z^{*}_{\Delta Au}>2$) (Fig. 12A). Thus, samples collected from the open-pit (n=170) have an average $Z^{*}_{\Delta Au}$ value of 3.2, which corresponds to an average enrichment factor (Δ_{Au}) of 690 relative to the least-altered samples. The distribution of high $Z^{*}_{\Delta Au}$ values (*i.e.*, $Z^{*}_{\Delta Au}>1$) extends beyond the limits of the deposit and defines a semi-continuous halo oriented parallel to the S_2 foliation.

548 Significantly, the anomalous areas defined by Au mass gains are not limited to the deposit, and also include
549 the main hydrothermal centers and prospects in the district, namely the Cartier, Radium, Alpha and Bravo
550 zones (Figs. 2 and 12A).

551 The mass change anomalies defined by pathfinder trace elements associated with gold mineralization
552 are illustrated in Figure 12 B to G. They show that the spatial distributions of mass change values for Te,
553 W, and Ag delineate district-scale alteration footprints around the Canadian Malartic deposit (Fig. 12B-D).
554 The mass gains calculated for these elements are generally highest within the area of the open-pit, and
555 decrease with distance away from the deposit (Fig. 12B-D). The Te, W and Ag anomalies contrast markedly
556 with the background values; samples from the open-pit (n=170) display pronounced mass gains compared
557 to the background metasedimentary rocks, with average $Z^*_{\Delta Te}$, $Z^*_{\Delta W}$ and $Z^*_{\Delta Ag}$ values reaching 2.9, 2.3 and
558 2.7, respectively (Fig. 12B-D). These values correspond to average Δ_{Te}, Δ_W and Δ_{Ag} enrichment factors of
559 35.8, 23.4 and 10.6, respectively. The mass gain distributions for these elements delineate alteration
560 envelopes surrounding the deposit that extend semi-continuously along strike for >10 kilometers (Fig.
561 12B-D). The geochemical anomalies delineated by Te, W and Ag correspond closely to the dispersion halo
562 outlined by the gold mass gains. Because it is not affected by false positive anomalies related to outliers,
563 W (and to a lesser extent Ag) displays the most consistent pathfinder footprint across the district (Fig.
564 12B-D).

565 The distributions of mass change values for As (Δ_{As}), Be (Δ_{Be}), Sb (Δ_{Sb}) and Pb (Δ_{Pb}) also include
566 positive anomalies associated with gold mineralization (Fig. 12E-H). Arsenic and Sb display moderate
567 enrichments in metasedimentary rocks of the immediate deposit area compared to the least-altered
568 equivalent metasedimentary rocks, and correspond to average $Z^*_{\Delta As}$ and $Z^*_{\Delta Sb}$ values of 0.9 and 0.8,
569 respectively (n=170); the anomalies for these elements extend towards the southeast in the direction of the
570 Bravo zone ($Z^*_{\Delta As}$ and $Z^*_{\Delta Sb}$ >1) (Fig. 12E,G). The distribution of Be mass change values (Δ_{Be}) outlines a
571 geochemical zonation with respect to the deposit, which is partially masked by a number of false anomalies
572 to the south and west of the district (Fig. 12F). Although the highest Pb enrichment (Δ_{Pb}) occurs within and
573 adjacent to the deposit, the distribution of Pb mass change values is relatively erratic across the district (Fig.
574 12H).

575 The spatial distribution of mass change values for mobile alkali and volatile parameters such as CO_2, S,
576 K_2O and LOI is presented in Figure 12I-L. Significantly, CO_2 and S display strong enrichments in the

deposit area, as shown by average $Z^*_{\Delta CO2}$ and $Z^*_{\Delta S}$ open-pit values of 1.6 and 1.4, respectively (n=170). These mass gains also delineate a broad S_2-parallel halo beyond the deposit, which is characterized by local enrichments ($Z^*_{\Delta CO2}$ and $Z^*_{\Delta S}$ >1) that coincide with the locations of other gold prospects in the district (*e.g.*, the Cartier, Radium, Alpha and Bravo zones) (Fig. 12I-J). The distribution of K_2O mass change values includes a positive lithogeochemical anomaly that is mainly restricted to the hydrothermally-altered rocks in the deposit area (Fig. 12K). Despite its relatively limited spatial extent, the potassium alteration halo stands out strongly from the background metasedimentary rocks, as shown by elevated values of $Z^*_{\Delta K2O}$ (1.2) for samples from within the open-pit (Fig. 12K). The few K_2O anomalies ($Z^*_{\Delta K2O}$ >1) outside the deposit correspond to weakly mineralized hydrothermal centers (*e.g.*, Cartier, Radium, Alpha and Bravo zones). The mass change values for LOI also identify a laterally extensive anomaly that extends parallel to the S_2 foliation along the Cadillac-Larder Lake Fault Zone (Fig. 12L). This anomaly is interpreted to mainly record the effects of carbonate and sulfide alteration, as shown by the high degree of overlap with the distribution of CO_2 and S mass changes (Fig. 12I-J,L).

9. Discussion

9.1. Mineralogical controls on hydrothermal alteration

Whole-rock lithogeochemical data provide a means with which to evaluate the mineralogical controls on hydrothermal alteration. In principle, this information can be used to identify the mineralogical changes that produce the zonation of alteration features around major hydrothermal systems. At Canadian Malartic, molar element ratio analysis indicates that there was a progressive decrease in alkali alteration away from the main fluid pathways (manifested by decreasing gradients of K/Al and Na/Al; Fig. 11). These results reflect the transition from proximal microcline±albite-(phlogopite) to distal biotite±phengite-microcline-albite alteration assemblages. As such, the stabilization of microcline at the expense of white mica in the proximal alteration assemblage is consistent with an increase in potassium metasomatism towards the fluid corridors (see Gaillard et al., 2018), and can be described by the reaction:

$$\underset{\text{white mica}}{KAl_3Si_3O_{10}(OH)_2} + 6\ SiO_2 + 2\ K^+ = 3\ \underset{\text{microcline}}{KAlSi_3O_8} + 2\ H^+ \qquad (6)$$

Hydrothermal alteration at Canadian Malartic is also characterized by a progressive increase in sulfur concentration adjacent to the fluid pathways (Fig. 8). The correlation between Δ_S and Δ_{K2O} mass changes (r=0.56) suggests a mineralogical coupling between sulfidation and potassic alteration (Fig. 10). Indeed,

606 the increase in pyrite alteration proximal to the fluid corridors is accompanied by an increase in microcline
607 at the expense of biotite (see Gaillard et al., 2018), probably in response to the reaction:

608 $KFe_3AlSi_3O_{10}(OH)_2 + 6\ H_2S + 1.5\ O_2 = KAlSi_3O_8 + 3\ FeS_2 + 7H_2O$ (7)
609 biotite microcline pyrite

610 In addition to sulfidation, hydrothermal alteration of the metasedimentary rocks involved the progressive
611 replacement of plagioclase (oligoclase) by albite and microcline. Because Ca was only weakly enriched
612 during alteration (Δ_{CaO} =1.20 in altered rocks), it is inferred that Ca in carbonates (calcite and Fe-dolomite)
613 was sourced mainly by the breakdown of oligoclase to albite (or microcline), as described by the reaction:

614 $Na_{0.72}Ca_{0.27}Si_{2.74}Al_{1.26}O_8 + 0.54\ Na^+ + 1.04\ SiO_2 + 0.27\ CO_2 + 0.27\ H_2O = 1.26\ NaAlSi_3O_8 + 0.27\ CaCO_3 + 0.54\ H^+$ (8)
615 oligoclase quartz albite calcite

616 This association between alkali alteration (K and Na) and carbonatization is reflected by the correlation
617 between Δ_{CO2} and $\Delta_{K2O+Na2O}$ mass changes (r=0.56), and was also documented by De Souza et al. (2019)
618 using carbonation indices. A weak enrichment in Na (Δ_{Na2O} =1.12 in altered rocks), however, suggests that
619 most of the Na involved in albitization was locally derived, and may have been released during replacement
620 of oligoclase by microcline (Helt et al., 2014; Gaillard et al., 2018). These observations indicate that the
621 alteration assemblage was controlled to a large extent by the host-rock composition. As such, alkali meta-
622 somatism was likely limited by the Al content of the rock, as K- and Na-bearing phases in the alteration
623 assemblage have alkali/aluminum molar element ratios ≤ 1 (Mathieu, 2018).

624 The above alteration (Reactions 6, 7 and 8) records a progressive increase in fO_2, $\sum aS$ and pH conditions
625 with increasing fluid-rock interaction. Consequently, the mineralogical changes that characterize alkali
626 metasomatism also contribute to the delineation of a sulfidation-oxidation halo around the fluid pathways,
627 in agreement with the conclusions of Gaillard et al. (2018). These changes also provide evidence that the
628 ore-forming fluids were oxidized, and potassium- and sulfur-rich.

629 ***9.2. Controls on the distribution of the metasomatic processes***

630 The results of the mass change calculations were used to outline metasomatic haloes associated with
631 ore-formation (Fig. 12). The lithogeochemical anomalies display large variations in size and intensity for
632 the different elements, which reflect the composition of the mineralizing fluids, the composition of the host
633 rocks and the mobility of alteration-related elements. The above notwithstanding, the alteration haloes
634 defined by the different elements all take the form of elongate envelopes that extend parallel to the main
635 (S_2) foliation (Fig. 12).

636 The spatial distribution of mass transfer depends on several factors, foremost among which are the
637 structures that controlled the circulation of the mineralizing fluids. At Canadian Malartic, the main ore-
638 stage is interpreted to have been synchronous with the D_2 deformation event. Indeed, the ore zones display
639 a strong spatial association with D_2 structures including the Sladen Fault, and the NW-SE deformation
640 zones (Fig. 3; Sansfaçon, 1986; De Souza et al., 2016). At the district scale, this association is manifested
641 by a distribution of gold showings (weakly mineralized zones) parallel to the S_2 foliation (Fig. 2). Most of
642 the lithogeochemical anomalies, notably those delineated by pathfinder trace elements, reflect this structural
643 control and form elongate haloes that extend parallel to the S_2 fabric (Fig. 12).

644 The geometry of the metasomatic haloes may also be affected by the superposition of metamorphic
645 and/or deformation events. At Canadian Malartic, gold mineralization is interpreted to have occurred early-
646 to syn-peak metamorphism (M_2) (Gaillard et al., 2018). For this reason, it is possible that the alteration
647 footprint associated with ore-formation was modified during metamorphism, which increased in grade from
648 upper greenschist facies adjacent to the deposit, to mid-amphibolite facies a few kilometers to the south
649 (Fig. 2). Most significantly, the transition from greenschist to amphibolite facies is generally associated
650 with a series of devolatilization reactions, which typically coincide with a release of sulfur due to the
651 conversion of pyrite to pyrrhotite (Pitcairn et al., 2006; Phillips and Powell, 2010; Gaillard et al., in review).
652 The latter may also play a role in the liberation of pyrite-hosted trace metals (*e.g.*, Au and related elements)
653 to the metamorphic fluids (Large et al., 2009; Pitcairn et al., 2010). In the Malartic district, devolatilization
654 reactions associated with increasing metamorphic grade likely contributed to a southward decrease in the
655 concentrations of these elements in the background metasedimentary rocks (Fig. 12). Thus, loss on ignition
656 (LOI), sulfur and carbon, as well as metals liberated during pyrite (*e.g.*, Au, As, Te, Bi) and/or Fe-Ti oxide
657 (*e.g.*, W, Sb) breakdown reactions (prograde) represent components that may have been mobilized along
658 the metamorphic gradient.

659 ### *9.3. Implications for mineral exploration*

660 The results of the mass transfer calculations provide evidence of a progressive increase in the concen-
661 trations of CO_2-S-K_2O and LOI, as well as Au-Te-W-Ag-(As-Be-Sb-Bi-Mo-Pb) from background to distal
662 and proximal alteration zones (Figs. 8-9; Appendix 2). The zones of enrichment correspond to metasomatic
663 haloes around the deposit that identify the domains of hydrothermal fluid-rock interaction in the Malartic
664 district (Fig. 12). The statistical approach employed in this study provided a rigorous means of constraining

665 the magnitude and extent of the lithogeochemical haloes. Here, we use this information to identify the
666 parameters that are likely to provide the most reliable vectors towards gold mineralization.

667 The pathfinder elements define extensive alteration footprints around the Canadian Malartic deposit,
668 that contrast sharply with the background metasedimentary rocks (Fig. 12A-G). The anomalies delineated
669 by Au, Te, W and Ag constitute the largest metasomatic haloes, reaching up to 10 km in length and 2 km
670 in width (Fig. 12A-D). Because they display a strong metasomatic signal and are only weakly affected by
671 outliers, W, and to a lesser extent, Te and Ag, provide the best vectors towards gold mineralization.
672 In contrast, other pathfinder elements, including As, Be and Sb, delineate asymmetric haloes around the
673 deposit, and display several false positive anomalies, thereby limiting their utility in vectoring towards ore
674 (Fig. 12E-H). Carbon, S and LOI outline district-scale geochemical haloes enveloping gold mineralization.
675 However, the presence of outliers that obscure gradients toward hydrothermal centers also limits their
676 applicability as regional vectors to mineralization (Fig. 12I-J,L). Finally, the potassic halo interpreted from
677 K_2O enrichment provides a useful proxy for hydrothermal alteration, although it is mainly restricted to the
678 immediate area of the deposit (Fig. 12K).

679 The mass transfer data for the Malartic district identify compositional parameters that potentially can be
680 applied more widely in exploring for gold in metamorphic terranes. The Au-Te-W-Ag-(As-Sb-Bi-Mo-Pb)
681 signature of the ore assemblage is remarkably similar to that of other intrusion-related and orogenic-type
682 gold deposits (Robert and Poulsen, 1997; Brauhart et al., 2017). Indeed, W, Te and Ag have also been
683 shown to provide vectors toward gold mineralization in the Red Lake (Stock, 2012) and Norseman-Wiluna
684 (Eilu and Groves, 2001; Prendergast, 2007) greenstone belts, and in the Lachlan fold belt (Bierlein et al.,
685 2000). In these locations, pathfinder elements were used to detect the cryptic effects of alteration a few tens
686 of meters, and more rarely up to several kilometers away from the fluid corridors.

687 The nature of hydrothermal alteration varies as a function of host-rock lithology (Bierlein et al., 2000).
688 In the Malartic district, a companion study by Perrouty et al. (2019) demonstrated that mafic dykes consti-
689 tute a chemically sensitive lithology with which to assess alteration. The lithogeochemical anomalies in the
690 mafic dykes differ in magnitude and spatial distribution from those in the metasedimentary rocks in several
691 ways. For example, carbon and alkali elements (K, Cs, Rb) delineate larger anomalies in the mafic dykes,
692 whereas pathfinder element (W, Te, Ag) anomalies generally extend further in the metasedimentary rocks.
693 These observations suggest a strong lithological control on the saturation and precipitation of species in the

ore-fluid, implying that the detection of cryptic alteration can be facilitated by employing multiple litho-types selected from those that are most reactive.

10. Conclusions

The results of this study provide compelling evidence that whole-rock lithogeochemistry is a valuable tool for mapping the intensity and distribution of hydrothermal alteration related to gold mineralization. By mapping the distribution of the mass changes, it is possible to gain insights into the paths taken by the hydrothermal fluids responsible for ore-formation, and to identify parameters that could serve as vectors towards gold mineralization. The signature of the Canadian Malartic mineralized system is characterized by strong enrichments in CO_2-S-K_2O-LOI, as well as Au-Te-W-Ag-(As-Be-Sb-Bi-Mo-Pb), that increase with decreasing distance to gold mineralization. Molar element ratio analysis was also shown to provide a reliable method for assessing the mineralogical controls on alkali metasomatism (K and Na), and in the case of the Malartic district, was used to document a progressive increase in the proportions of microcline and albite adjacent to fluid pathways (at the expense of oligoclase, biotite and white mica).

Enrichment patterns defined by pathfinder elements outline broad lithogeochemical anomalies around the deposit, and were used to document hydrothermal fluid-rock interaction in the district. The anomalies correspond to elongate alteration haloes oriented parallel to the foliation (S_2) that extend several kilometers laterally from the deposit. The ore-associated elements Au, W, Te and Ag delineate the largest anomalies, and define a semi-continuous alteration footprint approximately 10 km in length and 2 km in width. These findings demonstrate that lithogeochemistry provides a valuable vectoring tool for gold mineralization in metamorphic terranes, which can be used to recognize even cryptic alteration associated with ore-forming processes at the district-scale.

Acknowledgements

Funding for this study was provided by the Natural Sciences and Engineering Council (NSERC) and the Canada Mining Innovation Council (CMIC) through the collaborative research and development program. We are grateful to Canadian Malartic Corporation for logistical support and assistance during fieldwork. N. Piette-Lauzière, P. Lypaczewski, T. Raskevicius and C. L.-Bérubé participated in the fieldwork and sample collection. E. Grunsky provided essential guidance on data analysis and statistical methods. Our fellow researchers of the NSERC-CMIC Footprints project shared important observations from their own investigations and gave us continuous support: S. Piercey, R. Wares, M. Bardoux, G. Beaudoin, D. Béziat, H. Poulsen, the late K. Kyser, C. Guilmette, F. Robert, A. Galley and M. Lesher. We also benefitted from discussions with researchers of the TGI-4 project, S. De Souza, B. Dubé and P. Mercier-Langevin. The authors thank guest editor O. Kreuzer, D. Lentz, and an anonymous reviewer for constructive comments on the manuscript. Finally, we gratefully acknowledge the valuable assistance and feedback provided by industry sponsors. NSERC-CMIC Mineral Exploration Footprints Project Contribution 193.

REFERENCES

Aitchison, J., 1986, The Statistical Analysis of Compositional Data. Monographs on statistics and applied probability. Chapman & Hall, Ltd. London, UK, 416 p.

Ayer, J., Amelin, Y., Corfu, F., Kamo, S., Ketchum, J., Kwok, K., and Trowell, N., 2002, Evolution of the southern Abitibi greenstone belt based on U–Pb geochronology: autochthonous volcanic construction followed by plutonism, regional deformation and sedimentation: Precambrian Research, v. 115, p. 63-95.

Ayer, J. A., Thurston, P. C., Bateman, R., Dubé, B., Gibson, H. L., Hamilton, M. A., Hathway, B., Hocker, S. M., Houlé, M. G., Hudak, G., Ispolatov, V. O., Lafrance, B., Lesher, C. M., MacDonald, P. J., Péloquin, A. S., Piercey, S. J., Reed, L. E., and Thompson, P. H., 2005, Overview of results from the Greenstone Architecture Project: Discover Abitibi Initiative: Ontario Geological Survey, Open File Report 6154, 146 p.

Beaudoin, G., and Raskevicius, T., 2014, Constraints on the genesis of the Archean oxidized, intrusion-related Canadian Malartic gold deposit, Québec, Canada - A discussion: Economic Geology, v. 109, p. 2067-2068.

Bedeaux, P., Mathieu, L., Pilote, P., Rafini, S., and Daigneault, R., 2018, Origin of the Piché Structural Complex and implications for the early evolution of the Archean crustal-scale Cadillac - Larder Lake Fault Zone, Canada: Canadian Journal of Earth Sciences, v. 55, p. 905-922.

Bedeaux, P., Pilote, P., Daigneault, R., and Rafini, S., 2017, Synthesis of the structural evolution and associated gold mineralization of the Cadillac Fault, Abitibi, Canada: Ore Geology Reviews, v.82, p. 49-69

Benn, K., Miles, W., Ghassemi, M. R., and Gillett, J., 1994, Crustal structure and kinematic framework of the northwestern Pontiac Subprovince, Quebec: an integrated structural and geophysical study: Canadian Journal of Earth Sciences, v. 31, p. 271-281.

Bierlein, F. P., Arne, D. C., McKnight, S., Lu, J., Reeves, S., Besanko, J., Marek, J., and Cooke, D., 2000, Wall-Rock petrology and geochemistry in alteration halos associated with mesothermal gold mineralization, Central Victoria, Australia: Economic Geology, v. 95, p. 283-311.

Bierlein, F. P., Fuller, T., Stüwe, K., Arne, D. C., and Keays, R. R., 1998, Wallrock alteration associated with turbidite-hosted gold deposits: examples from the Palaeozoic Lachlan Fold Belt in central Victoria, Australia: Ore Geology Reviews, v. 13, p. 345-380.

Bleeker, W., 2015, Synorogenic gold mineralization in granite-greenstone terranes: the deep connection between extension, major faults, synorogenic clastic basins, magmatism, thrust inversion, and long-term preservation: Targeted Geoscience Initiative 4: Contributions to the Understanding of Precambrian Lode Gold Deposits and Implications for Exploration, B. Dubé and P. Mercier-Langevin (eds.); Geological Survey of Canada, Open File 7852, p. 27-47.

Brauhart, C. W., Grunsky, E. C., and Hagemann, S. G., 2017, Magmato-hydrothermal space: A new metric for geochemical characterisation of metallic ore deposits: Ore Geology Reviews, v. 86, p. 867-895.

Cai, G., Guo, F., Liu, X., Sui, S., Li, C., and Zhao, L., 2008, Geochemistry of Neogene sedimentary rocks from the Jiyang basin, North China Block: The roles of grain size and clay minerals: Geochemical Journal, v. 42, p. 381-402.

Camiré, G. E., and Burg, J. P., 1993, Late Archaean thrusting in the northwestern Pontiac Subprovince, Canadian Shield: Precambrian Research, v. 61, p. 51-66.

Camiré, G. E., Laflèche, M. R., and Ludden, J. N., 1993, Archaean metasedimentary rocks from the north-western Pontiac Subprovince of the Canadian shield: chemical characterization, weathering and modelling of the source areas: Precambrian Research, v. 62, p. 285-305.

Card, K. D., and Poulsen, K. H., 1998, Geology and mineral deposits of the Superior province of the Canadian Shield: Geology of Canada Series no. 7, v. in, Geology of the Precambrian Superior and Grenville provinces and Precambrian fossils in North America, p. 15-204.

Chown, E. H., Harrap, R., and Moukhsil, A., 2002, The role of granitic intrusions in the evolution of the Abitibi belt, Canada: Precambrian Research, v. 115, p. 291-310.

Clark, M. E., Carmichael, D. M., Hodgson, C. J., and Fu, M., 1989, Wall-rock alteration, Victory gold mine, Kambalda, Western Australia: processes and P-T-X(CO_2) conditions of metasomatism: Economic Geology Monograph 6, p. 445-459.

Daigneault, R., Mueller, W. U., and Chown, E. H., 2002, Oblique Archean subduction: accretion and exhumation of an oceanic arc during dextral transpression, Southern Volcanic Zone, Abitibi Subprovince Canada: Precambrian Research, v. 115, p. 261-290.

Davies, J. F., and Whitehead, R. E., 1994, Molar ratios in the study of unaltered and hydrothermally altered greywackes and shales: Chemical Geology, v. 111, p. 85-100.

Davies, J. F., and Whitehead, R. E., 2006, Alkali-Alumina and MgO-Alumina molar ratios of altered and unaltered rhyolites, Exploration and Mining Geology, v. 15, p. 75-88.

Davis, D. W., 2002, U–Pb geochronology of Archean metasedimentary rocks in the Pontiac and Abitibi subprovinces, Quebec, constraints on timing, provenance and regional tectonics: Precambrian Research, v. 115, p. 97-117.

Davis, W. J., Lacroix, S., Gariépy, C., and Machado, N., 2000, Geochronology and radiogenic isotope geochemistry of plutonic rocks from the central Abitibi subprovince: significance to the internal subdivision and plutono-tectonic evolution of the Abitibi belt: Canadian Journal of Earth Sciences, v. 37, p. 117-133.

De Souza, S., Dubé, B., McNicoll, V. J., Dupuis, C., Mercier-Langevin, P., Creaser, R. A., and Kjarsgaard, I. M., 2015, Geology, hydrothermal alteration, and genesis of the world-class Canadian Malartic stockwork-disseminated Archean gold deposit, Abitibi, Quebec: Targeted Geoscience Initiative 4: Contributions to the Understanding of Precambrian Lode Gold Deposits and Implications for Exploration, B. Dubé and P. Mercier-Langevin (eds.); Geological Survey of Canada, Open File 7852, p. 113-126.

De Souza, S., Dubé, B., McNicoll, V. J., Dupuis, C., Mercier-Langevin, P., Creaser, R. A., and Kjarsgaard, I. M., 2016, Geology and hydrothermal alteration of the world-class Canadian Malartic gold deposit: genesis of an Archean stockwork-disseminated gold deposit in the Abitibi Greenstone Belt, Québec: Reviews in Economic Geology, v. 19, 29 p.

De Souza, S., Dubé, B., Mercier-Langevin, P., McNicoll, V., Dupuis, C., and Kjarsgaard, I. M., 2019, Hydrothermal Alteration Mineralogy and Geochemistry of the Archean World-Class Canadian Malartic Disseminated-Stockwork Gold Deposit, Southern Abitibi Greenstone Belt, Quebec, Canada: Economic Geology, v. 114, p. 1057-1094.

Derry, D. R., 1939, The geology of the Canadian Malartic gold mine, N. Quebec: Economic Geology, v. 34, p. 495-523.

Desrochers, J.-P., and Hubert, C., 1996, Structural evolution and early accretion of the Archean Malartic Composite Block, southern Abitibi greenstone belt, Quebec, Canada: Canadian Journal of Earth Sciences, v. 33, p. 1556-1569.

Dimroth, E., Imreh, L., Rocheleau, M., and Goulet, N., 1982, Evolution of the south-central part of the Archean Abitibi Belt, Quebec. Part I: Stratigraphy and paleogeographic model: Canadian Journal of Earth Sciences, v. 19, p. 1729-1758.

Eilu, P., and Mikucki, E. J., 1998, Alteration and primary geochemical dispersion associated with the Bulletin lode-gold deposit, Wiluna, Western Australia: Journal of Geochemical Exploration, v. 63, p. 73-103.

Eilu, P., Mathison, C. I., Groves, D. I., and Allardyce, W., 1999, Atlas of alteration assemblages, styles and zoning in orogenic lode-gold deposits in a variety of host rock and metamorphic settings: Nedlands, Geology Publications, UWA Extension, University of Western Australia, 50 p.

Eilu, P., and Groves, D. I., 2001, Primary alteration and geochemical dispersion haloes of Archaean orogenic gold deposits in the Yilgarn Craton: the pre-weathering scenario: Geochemistry: Exploration, Environment, Analysis, v. 1, p. 183-200.

Eilu, P., Mikucki, J. E., and Dugdale, L. A., 2001, Alteration zoning and primary geochemical dispersion at the Bronzewing lode-gold deposit, Western Australia: Mineralium Deposita, v. 36, p. 13-31.

Fallara, F., Simon-Ross, P., and Sansfaçon, R., 2000, Caractérisation géochimique, pétrographique et structurale: nouveau modèle métallogénique du camp de Malartic: Géologie Québec, MB 2000-15, 111 p.

Feng, R., and Kerrich, R., 1992, Geodynamic evolution of the southern Abitibi and Pontiac terranes: evidence from geochemistry of granitoid magma series (2700-2630 Ma): Canadian Journal of Earth Sciences, v. 29, p. 2266-2286.

Finlow-Bates, T., and Stumpfl, E. F., 1981, The behaviour of so-called immobile elements in hydro-thermally altered rocks associated with volcanogenic submarine-exhalative ore deposits: Mineralium Deposita, v. 16, p. 319-328.

Frieman, B. M., Kuiper, Y. D., Kelly, N. M., Monecke, T., and Kylander-Clark, A., 2017, Constraints on the geodynamic evolution of the southern Superior Province: U-Pb LA-ICP-MS analysis of detrital zircon in successor basins of the Archean Abitibi and Pontiac subprovinces of Ontario and Quebec, Canada: Precambrian Research, v. 292, p. 398-416.

Gaillard, N., Williams-Jones, A. E., Clark, J. R., Lypaczewski, P., Salvi, S., Perrouty, S., Piette-Lauzière, N., Guilmette, C., and Linnen, R. L., 2018, Mica composition as a vector to gold mineralization: Deciphering hydrothermal and metamorphic effects in the Malartic district, Quebec: Ore Geology Reviews, v. 95, p. 789-820.

Gaillard, N., Williams-Jones, A. E., Clark, J. R., Salvi, S., Perrouty, S., and Linnen, R. L., in review, Reconstructing hydrothermal and metamorphic paths using textural, modal and mineral-chemical features of pyrite and pyrrhotite: Vectoring to gold mineralization in the Malartic district, Québec.

Gaillard, N., Williams-Jones, A. E., Clark, J. R., Salvi, S., Béziat, D., Lypaczewski, P., Perrouty, S., and Linnen, R. L., 2015, Mineralogical and geochemical vectors to ore: the alteration halo of the Canadian Malartic gold deposit.: Proceedings of the 13th, Biennial SGA Meeting, Nancy, France, v. 2, p. 461-464.

Gao, J.-F., Jackson, S. E., Dubé, B., Kontak, D. J., and De Souza, S., 2015, Genesis of the Canadian Malartic, Côté Gold, and Musselwhite gold deposits: insights from LA-ICP-MS element mapping of pyrite: Targeted Geoscience Initiative 4: Contributions to the Understanding of Precambrian Lode Gold Deposits and implications for exploration. B. Dubé and P. Mercier-Langevin (eds.); Geological Survey of Canada, Open File 7852, p. 157-175.

Ghassemi, M. R., 1996, Tectonic evolution of the Late Archean Pontiac Subprovince, Superior Province, Canada: Structural, metamorphic and geochronological studies: Ph.D. thesis, University of Ottawa, 314 p.

Goldfarb, R. J., Baker, T., Dube, B., Groves, D. I., Hart, C. J. R., and Gosselin, P., 2005, Distribution, character, and genesis of gold deposits in metamorphic terranes: Economic Geology and the bulletin of the Society of Economic Geologists, 100th Anniversary Volume 1905-2005; In: Hedenquist, J.W., Thompson, J.F.H., Goldfarb, R.J., and Richards, J.P. (eds.), p. 407–450.

Goulet, N., 1978, Stratigraphy and structural relationships across the Cadillac-Larder lake fault, Rouyn-Beauchastel area, Quebec: Ministère des Ressources Naturelles du Quebec, DP-602, 141 p.

Grant, J. A., 1986, The isocon diagram; a simple solution to Gresens' equation for metasomatic alteration: Economic Geology, v. 81, p. 1976-1982.

Gresens, R. L., 1967, Composition-volume relationships of metasomatism: Chemical Geology, v. 2, p. 47-65.

Gunning, H. C., and Ambrose, J. W., 1943, Région de Malartic, Québec: Commission géologique du Canada, Mémoire 222, 162 p. (12 feuilles).

Halley, S., Dilles, J. H., and Tosdal, R. M., 2015, Footprints: hydrothermal alteration and geochemical dispersion around porphyry copper deposits: SEG newsletter, v. 100, 7 p.

Helsel, D. R., 2005, Non-detects and data analysis: Statistics for censored environmental data, John Wiley & Sons, 250 p.

Helsel, D. R., and Gilliom, R. J., 1986, Estimation of distributional parameters for censored trace level water quality data: 1. Estimation techniques: Water Resources Research, v. 22, p. 147-155.

Helt, K. M., Williams-Jones, A. E., Clark, J. R., Wing, B. A., and Wares, R. P., 2014, Constraints on the Genesis of the Archean Oxidized, Intrusion-Related Canadian Malartic Gold Deposit, Quebec, Canada: Economic Geology, v. 109, p. 713-735.

Hron, K., Templ, M., and Filzmoser, P., 2010, Imputation of missing values for compositional data using classical and robust methods: Computational Statistics & Data Analysis, v. 54, p. 3095-3107.

Hubert, C., Trudel, P., and Gélinas, L., 1984, Archean wrench fault tectonics and structural evolution of the Blake River Group, Abitibi Belt, Quebec: Canadian Journal of Earth Sciences, v. 21, p. 1024-1032.

Huston, C., and Juarez-Colunga, E., 2009, Guidelines for computing summary statistics for data-sets containing non-detects: Bulkley Valley Research Center, 178 p.

Imreh, L., 1984, Sillon de la Motte-Vassan et son avant-pays méridional; synthèse volcanologique, lithostratigraphique et gitologique: Ministère des Ressources Naturelles, The La Motte-Vassan Structure and its southern foreland; volcanologic, lithostratigraphic and economic synthesis, p. 72.

Issigonis, M. J., 1980, Occurrence of disseminated gold deposits in porphyries in Archean Abitibi belt, NW Quebec, Canada: Institution of Mining and Metallurgy London, Transactions, Section B: Applied Earth Sciences, v. 89, p. 157-158.

Knight, J. T., Ridley, J. R., and Groves, D. I., 2000, The Archean Amphibolite Facies Coolgardie Goldfield, Yilgarn Craton, Western Australia: Nature, Controls, and Gold Field-Scale Patterns of Hydrothermal Wall-Rock Alteration: Economic Geology, v. 95, p. 49-84.

Korzhinskii, D. S., 1968, The theory of metasomatic zoning: Mineralium Deposita, v. 3, p. 222-231.

Large, R. R., Danyushevsky, L., Hollit, C., Maslennikov, V., Meffre, S., Gilbert, S., Bull, S., Scott, R., Emsbo, P., Thomas, H., Singh, B., and Foster, J., 2009, Gold and Trace Element Zonation in Pyrite Using a Laser Imaging Technique: Implications for the Timing of Gold in Orogenic and Carlin-Style Sediment-Hosted Deposits: Economic Geology, v. 104, p. 635-668.

Libbey, R. B., and Williams-Jones, A. E., 2016, Lithogeochemical approaches in geothermal system characterization: An application to the Reykjanes geothermal field, Iceland: Geothermics, v. 64, p. 61-80.

Limpert, E., Stahel, W. A., and Abbt, M., 2001, Log-normal Distributions across the Sciences: Keys and Clues on the charms of statistics, and how mechanical models resembling gambling machines offer a link to a handy way to characterize log-normal distributions, which can provide deeper insight into variability and probability—normal or log-normal: That is the question: BioScience, v. 51, p. 341-352.

Lypaczewski, P., Rivard, B., Gaillard, N., Perrouty, S., Piette-Lauzière, N., Bérubé, C. L., and Linnen, R. L., 2019, Using hyperspectral imaging to vector towards mineralization at the Canadian Malartic gold deposit, Québec, Canada: Ore Geology Reviews, v. 111, 15 p.

MacLean, W. H., 1990, Mass change calculations in altered rock series: Mineralium Deposita, v. 25, p. 44-49.

MacLean, W. H., and Barrett, T. J., 1993, Lithogeochemical techniques using immobile elements: Journal of Geochemical Exploration, v. 48, p. 109-133.

MacLean, W. H., and Kranidiotis, P., 1987, Immobile elements as monitors of mass transfer in hydrothermal alteration; Phelps Dodge massive sulfide deposit, Matagami, Quebec: Economic Geology, v. 82, p. 951-962.

Madeisky, H. E., and Stanley, C. R., 1993, Lithogeochemical Exploration of Metasomatic Zones Associated with Volcanic-Hosted Massive Sulfide Deposits Using Pearce Element Ratio Analysis: International Geology Review, v. 35, p. 1121-1148.

Makvandi, S., Ghasemzadeh-Barvarz, M., Beaudoin, G., Grunsky, E. C., McClenaghan, M. B., Duchesne, C., and Boutroy, E., 2016, Partial least squares-discriminant analysis of trace element compositions of magnetite from various VMS deposit subtypes: Application to mineral exploration: Ore Geology Reviews, v. 78, p. 388-408.

Mathieu, L., 2018, Quantifying hydrothermal alteration: A review of methods: Geosciences (Switzerland), v. 8, 27 p.

McCuaig, T. C., Kerrich, R., Groves, D. I., and Archer, N., 1993, The nature and dimensions of regional and local gold-related hydrothermal alteration in tholeiitic metabasalts in the Norseman goldfields: the missing link in a crustal continuum of gold deposits?: Mineralium Deposita, v. 28, p. 420-435.

McDonough, W., and Sun, S. S., 1995, The composition of the Earth, p. 1050-1056.

Mishra, M., and Sen, S., 2011, Geochemical signatures for the grain size variation in the siliciclastics of Kaimur Group, Vindhyan Supergroup from Markundi ghat, Sonbhadra district, (U.P.), India: Geochemistry International, v. 49, p. 274-290.

Mortensen, J. K., and Card, K. D., 1993, U-Pb age constraints for the magmatic and tectonic evolution of the Pontiac Subprovince, Quebec: Canadian Journal of Earth Sciences, v. 30, p. 1970-1980.

Nesbitt, B. E., 1986a, Oxide-sulfide-silicate equilibria associated with metamorphosed ore deposits; Part I, Theoretical considerations: Economic Geology, v. 81, p. 831-840.

Nesbitt, B. E., 1986b, Oxide-sulfide-silicate equilibria associated with metamorphosed ore deposits; Part II, Pelitic and felsic volcanic terrains: Economic Geology, v. 81, p. 841-856.

Neumayr, P., Walshe, J., Hagemann, S., Petersen, K., Roache, A., Frikken, P., Horn, L., and Halley, S., 2008, Oxidized and reduced mineral assemblages in greenstone belt rocks of the St. Ives gold camp, Western Australia: vectors to high-grade ore bodies in Archaean gold deposits? Mineralium Deposita, v. 43, p. 363-371.

Palarea-Albaladejo, J., and Martín-Fernández, J. A., 2015, zCompositions - R package for multivariate imputation of left-censored data under a compositional approach: Chemometrics and Intelligent Laboratory Systems, v. 143, p. 85-96.

Palarea-Albaladejo, J., Martín-Fernández, J. A., and Buccianti, A., 2014, Compositional methods for estimating elemental concentrations below the limit of detection in practice using R: Journal of Geochemical Exploration, v. 141, p. 71-77.

Pearce, T. H., 1968, A contribution to the theory of variation diagrams: Contributions to Mineralogy and Petrology, v. 19, p. 142-157.

Perrouty, S., Gaillard, N., Piette-Lauzière, N., Mir, R., Bardoux, M., Olivo, G. R., Linnen, R. L., Bérubé, C. L., Lypaczewski, P., Guilmette, C., Feltrin, L., and Morris, W. A., 2017, Structural setting for Canadian Malartic style of gold mineralization in the Pontiac Subprovince, south of the Cadillac Larder Lake Deformation Zone, Québec, Canada: Ore Geology Reviews, v. 84, p. 185-201.

Perrouty, S., Linnen, R. L., Lesher, C. M., Olivo, G. R., Piercey, S. J., Gaillard, N., Clark, J. R., and Enkin, R. J., 2019, Expanding the size of multi-parameter metasomatic footprints in gold exploration: utilization of mafic dykes in the Canadian Malartic district, Québec, Canada: Mineralium Deposita, v. 54, p. 761-786.

Phillips, G. N., and Powell, R., 2010, Formation of gold deposits: a metamorphic devolatilization model: Journal of Metamorphic Geology, v. 28, p. 689-718.

Piercey, S. J., Ansdell, K., Beaudoin, G., Chouteau, M., Enkin, R. J., Gleeson, S., Hollings, P., Layton-Matthews, D., Lesher, C.M., Morris, B., Samson, I.M., et al., 2014, Sampling, Sample Processing, and Analytical Protocols, White Paper #3, v2014.07.11

Piette-Lauzière, N., 2017, Métamorphisme régional du nord-est de la Sous-province de Pontiac, Abitibi, Québec, Mémoire de Maîtrise en Sciences de la Terre, Université Laval, 280 p.

Piette-Lauzière, N., Guilmette, C., Bouvier, A., Perrouty, S., Pilote, P., Gaillard, N., Lypaczewski, P., Linnen, R. L., and Olivo, G. R., 2019, The timing of prograde metamorphism in the Pontiac Subprovince, Superior craton; implications for Archean geodynamics and gold mineralization: Precambrian Research, v. 320, p. 111-136.

Pilote, P., Daigneault, R., David, J., and McNicoll, V., 2015, Architecture of the Malartic, Piché and Cadillac groups and the Cadillac Fault: Geological revisions, new dates and interpretations, Ministère de l'Énergie et des Ressources Naturelles, 37 p.

Pitcairn, I. K., Olivo, G. R., Teagle, D. A. H., and Craw, D., 2010, Sulfide evolution during prograde metamorphism of the Otago and Alpine schists, New Zealand: The Canadian Mineralogist, v. 48, p. 1267-1295.

Pitcairn, I. K., Teagle, D. A. H., Craw, D., Olivo, G. R., Kerrich, R., and Brewer, T. S., 2006, Sources of Metals and Fluids in Orogenic Gold Deposits: Insights from the Otago and Alpine Schists, New Zealand: Economic Geology, v. 101, p. 1525-1546.

Powell, W. G., Hodgson, C. J., Hanes, J. A., Carmichael, D. M., Mcbride, S., and Farrar, E., 1995, $^{40}Ar/^{39}Ar$ geochronological evidence for multiple postmetamorphic hydrothermal events focused along faults in the southern Abitibi greenstone belt: Canadian Journal of Earth Sciences, v. 32, p. 768-786.

Prendergast, K., 2007, Application of lithogeochemistry to gold exploration in the St Ives goldfield, Western Australia: Geochemistry: Exploration, Environment, Analysis, v. 7, p. 99-108.

Rafini, S., 2014, Fiches descriptives de gites - Faille de Cadillac: Projet Consorem 2011-01 et 2012-01, 187 p.

Ricci-Lucchi, F., and Amorosi, A., 1978, Bedding and internal structures, Sedimentology: Berlin, Heidelberg, Springer Berlin Heidelberg, p. 85-98.

Ridley, J., Mikucki, E. J., and Groves, D. I., 1996, Archean lode-gold deposits: fluid flow and chemical evolution in vertically extensive hydrothermal systems: Ore Geology Reviews, v. 10, p. 279-293.

Robert, F., 2001, Syenite-associated disseminated gold deposits in the Abitibi greenstone belt, Canada: Mineralium Deposita, v. 36, p. 503-516.

Robert, F., and Poulsen, K. H., 1997, World-class Archaean gold deposits in Canada: An overview: Australian Journal of Earth Sciences, v. 44, p. 329-351.

Robert, F., Poulsen, K. H., Cassidy, K. F., and Hodgson, C. J., 2005, Gold Metallogeny of the Superior and Yilgarn Cratons: Economic Geology and the bulletin of the Society of Economic Geologists, 100th Anniversary Volume 1905-2005; In: Hedenquist, J.W.; Thompson, J.F.H.; Goldfarb, R.J.; and Richards, J.P. (eds.), p. 1001-1033.

Sansfaçon, R., 1986, The Malartic district: in Hubert, C., and Robert, F., eds., Structure and gold, Rouyn to Val d'Or, Québec: Geological Association of Canada-Mineralogical Association of Canada-Canadian Geophysical Union Joint Annual Meeting, Field Trip 14 Guidebook, Structure and gold, Rouyn to Val d'Or, Québec, p. 27-41.

Sansfaçon, R., Grant, M., and Trudel, P., 1987*a*, Géologie de la mine Barnat - Sladen Malartic - District de Val d'Or -: Série des manuscripts bruts - Direction Générale de l'Exploration Géologique et Minérale, MB 87-41, 73 p.

Sansfaçon, R., Grant, M., and Trudel, P., 1987*b*, Géologie de la mine Canadian Malartic - District de Val d'Or: Série des manuscripts bruts - Direction Générale de l'Exploration Géologique et Minérale, MB87-26, 50 p.

Sansfaçon, R., and Hubert, C., 1990, The Malartic Gold District, Abitibi greenstone belt, Québec: Geological setting, structure and timing of gold emplacement Barnat, East- Malartic, Canadian Malartic and Sladen Mines.: In: Rive, M., Verpealst, P., Gagnon, Y., Lulin, J.M., Riverin, G., Simard, A. (Eds.), The northwestern Quebec polymetallic belt: a summary of 60 years of mining exploration, Special Vol. 43., Canadian Institute of Mining and Metallurgy, p. 221–235.

Simard, M., Gaboury, D., Daigneault, R., and Mercier-Langevin, P., 2013, Multistage gold mineralization at the Lapa mine, Abitibi Subprovince: insights into auriferous hydrothermal and metasomatic processes in the Cadillac–Larder Lake Fault Zone: Mineralium Deposita, v. 48, p. 883-905.

Stanley, C. R., 2017, Molar Element Ratio Analysis of Lithogeochemical Data: A Toolbox for Use in Mineral Exploration and Mining: Proceedings of Exploration 17: Sixth Decennial International Conference on Mineral Exploration, edited by V. Tschirhart and M.D. Thomas, p. 471–494.

Stock, E. D., 2012, The mineralogical, geochemical and isotope characteristics of alteration, mineralization and metamorphism of the Red Lake Gold Mines, Ontario: Ph.D. thesis, University of British Columbia, 705 p.

Sutcliffe, R. H., Barrie, C. T., Burrows, D. R., and Beakhouse, G. P., 1993, Plutonism in the southern Abitibi Subprovince; a tectonic and petrogenetic framework: Economic Geology, v. 88, p. 1359-1375.

Thurston, P. C., Ayer, J. A., Goutier, J., and Hamilton, M. A., 2008, Depositional Gaps in Abitibi Greenstone Belt Stratigraphy: A Key to Exploration for Syngenetic Mineralization: Economic Geology, v. 103, p. 1097-1134.

Trudel, P., and Sauvé, P., 1992, Synthèse des caractéristiques géologiques des gisements d'or du district de Malartic: Direction Générale de l'Exploration Géologique et Minérale, MM 89-04, 126 p.

Warren, I., Simmons, S. F., and Mauk, J. L., 2007, Whole-Rock Geochemical Techniques for Evaluating Hydrothermal Alteration, Mass Changes, and Compositional Gradients Associated with Epithermal Au-Ag Mineralization: Economic Geology, v. 102, p. 923-948.

Whitbread, M. A., and Moore, C. L., 2004, Two lithogeochemical approaches to the identification of alteration patterns at the Elura Zn–Pb–Ag deposit, Cobar, New South Wales, Australia: use of Pearce Element Ratio analysis and Isocon analysis: Geochemistry: Exploration, Environment, Analysis, v. 4, p. 129-141.

Wilkinson, L., Cruden, A. R., and Krogh, T. E., 1999, Timing and kinematics of post-Timiskaming deformation within the Larder Lake - Cadillac deformation zone, southwest Abitibi greenstone belt, Ontario, Canada: Canadian Journal of Earth Sciences, v. 36, p. 627-647.

FIGURES

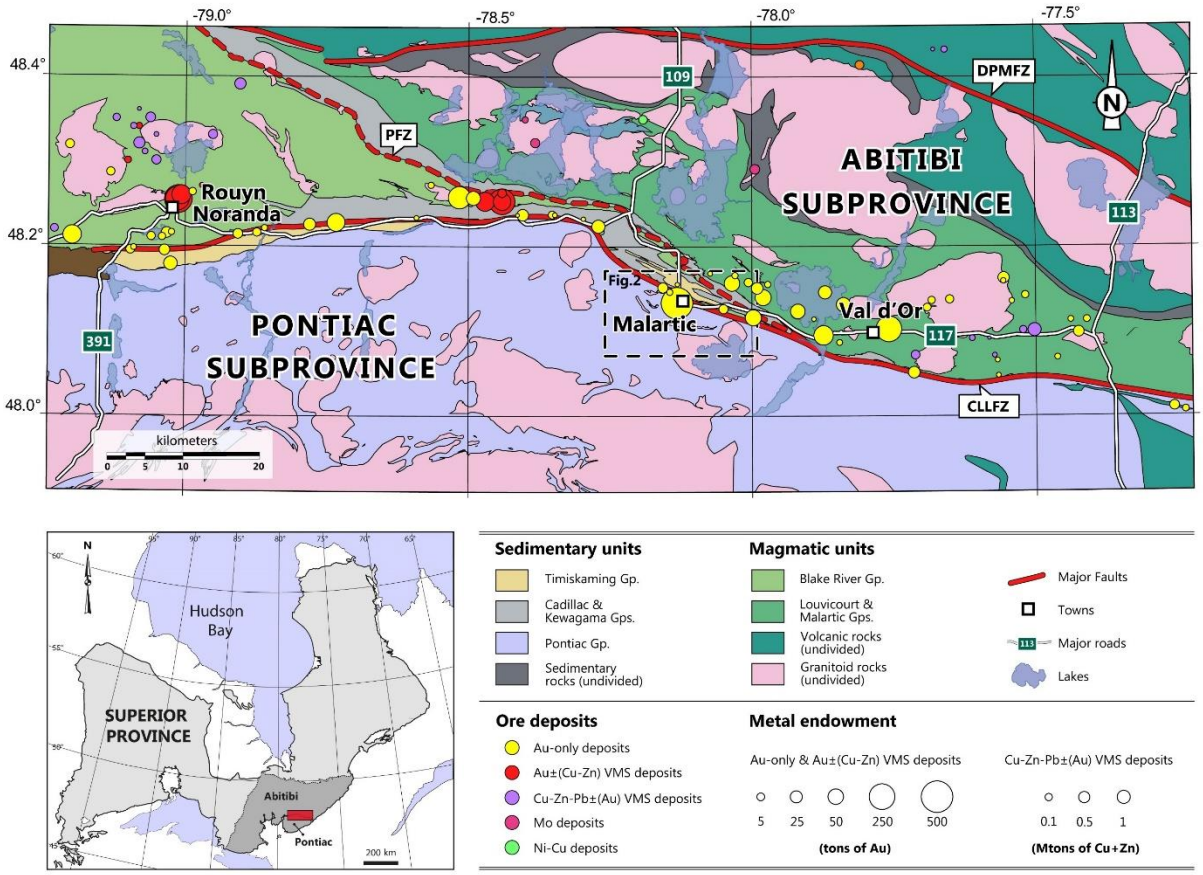

***Figure 1**: A regional lithostratigraphic map of the Abitibi and Pontiac subprovinces showing the locations of the main ore deposits along the Rouyn-Val d'Or segment (modified from Bedeaux et al., 2017; compiled from Hubert et al., 1984; Imreh, 1984; Desrochers and Hubert, 1996). Individual deposits are represented by colored circles that are scaled according to metal endowment, as calculated from past production and current reserve estimates (compiled from Rafini (2014), and references therein). Abbreviations: CLLFZ: Cadillac-Larder Lake Fault Zone; DPMFZ: Destor-Porcupine-Manneville Fault Zone; PFZ: Parfouru Fault Zone.*

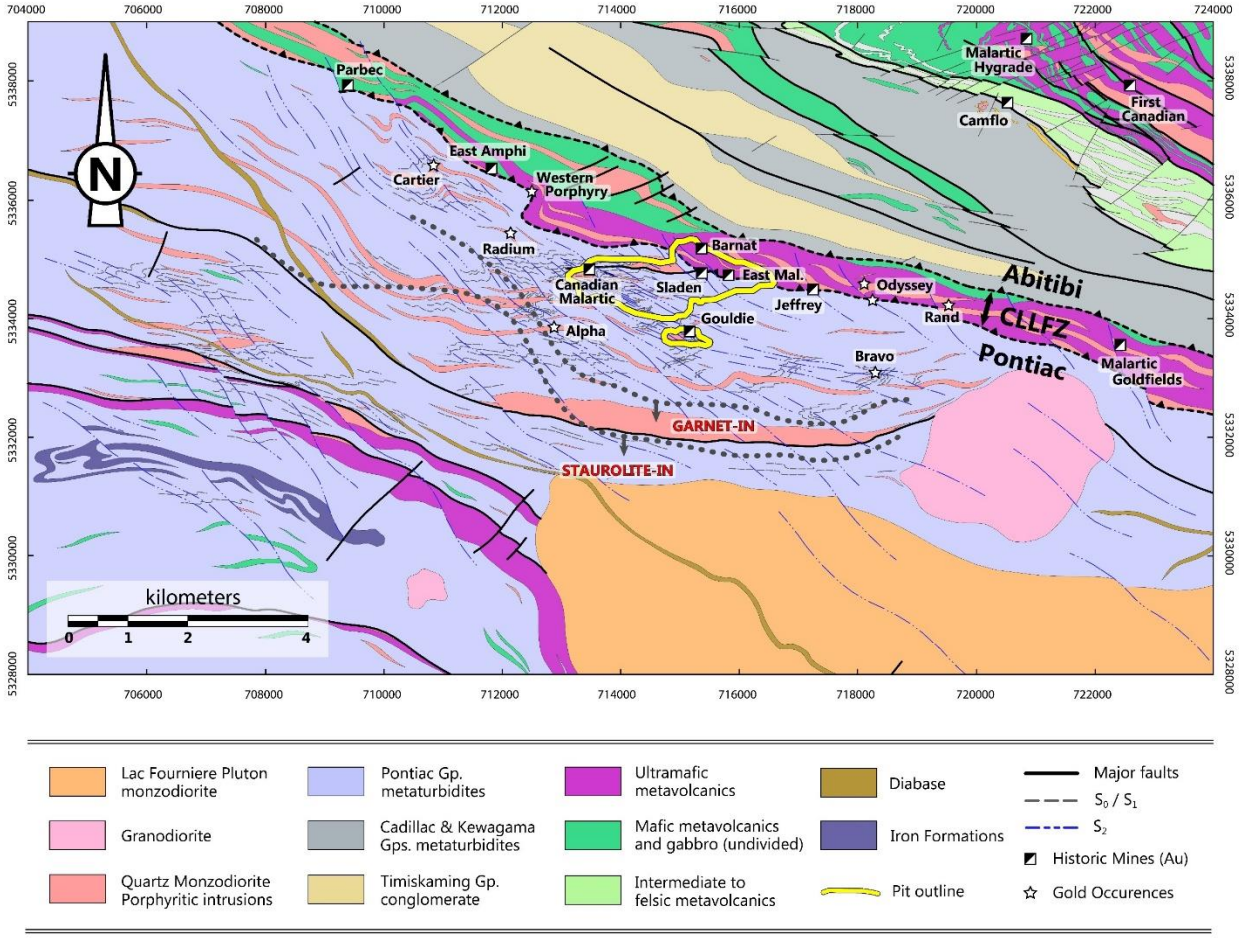

***Figure 2**: A lithostratigraphic map of the Malartic district showing the main structural, metamorphic and lithological features of the study area (modified from Perrouty et al., 2017; compiled from Derry, 1939; Gunning and Ambrose, 1943; Minerais Lac Limited maps; Sansfaçon et al., 1987a,b; Fallara et al., 2000; SIGEOM database, 2016; and references therein). The Canadian Malartic open-pit mine is delineated by a yellow line. The map also shows the locations of the past-producing mines and gold occurrences. UTM Coordinate system NAD83-17N. Abbreviation: CLLFZ: Cadillac-Larder Lake Fault Zone.*

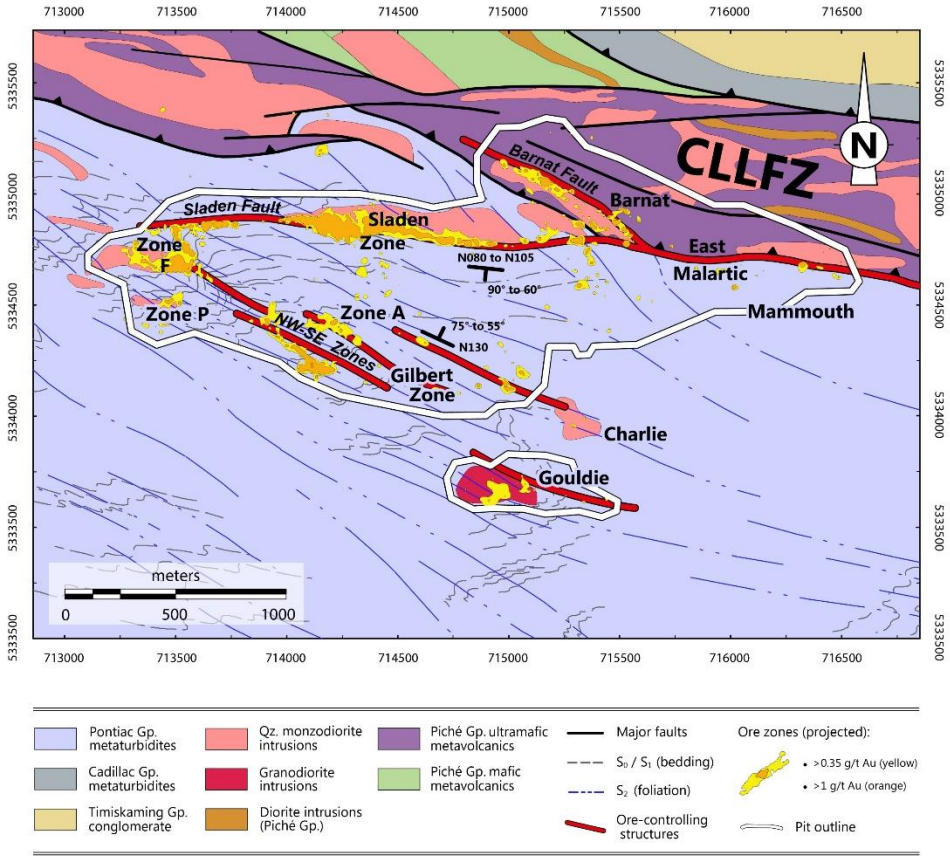

***Figure 3**: A geological map of the Canadian Malartic gold deposit (modified from Gaillard et al., 2018; compiled from MERN geological map CG-32D01D, Pilote, 2014; Perrouty et al., 2017; Canadian Malartic Corporation reports; and this study). Gold mineralized zones are projected from elevation z=300±10m. The ore distribution was controlled mainly by three structures, namely the Sladen and Barnat faults, and the NW-SE deformation zones. Abbreviation: CLLFZ: Cadillac-Larder Lake Fault Zone.*

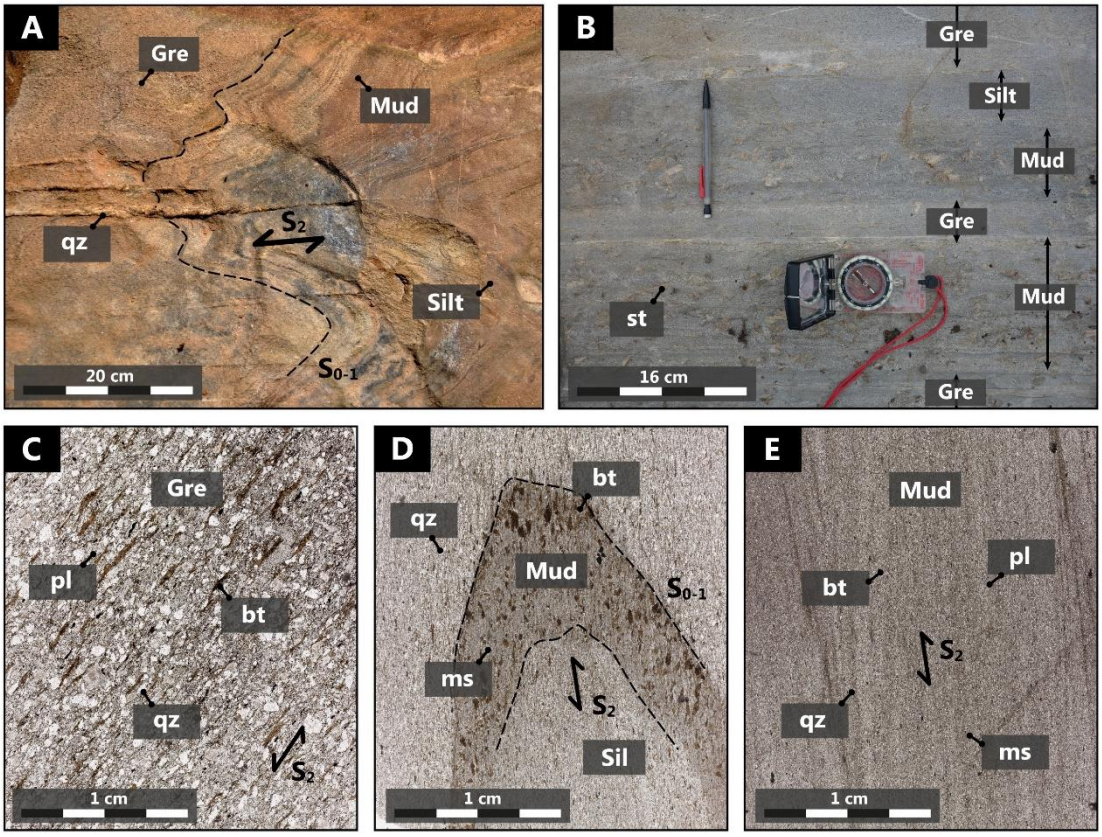

***Figure 4**: Features of the Pontiac Group metasedimentary rocks hosting the Canadian Malartic deposit. **A**: A flyschoid sequence composed of interstratified mudstone to greywacke beds. The rocks were affected by F_2 folding and display a strong pervasive axial-planar foliation (S_2). **B**: Local effects of the primary compositional variations on the mineralogy of the metamorphic assemblage in a planar-stratified turbiditic sequence. The staurolite porphyroblasts are restricted to the fine-grained pelitic beds (mudstone). **C**: A thin section image showing the textural characteristics of the greywacke. The clastic particles of quartz and plagioclase reach up to 1 mm in diameter. **D**: A thin section image of a micro-folded (F_2) sedimentary contact (S_{0-1}). White mica is developed preferentially in the finer-grained, more aluminous mudstone. **E**: A thin section image showing the textural characteristics of the mudstone. Detrital quartz and plagioclase grains are typically <50 µm across. Abbreviations: bt: biotite; Gre: greywacke; ms: muscovite; Mud: mudstone; pl: plagioclase; qz: quartz; Silt: siltstone; st: staurolite.*

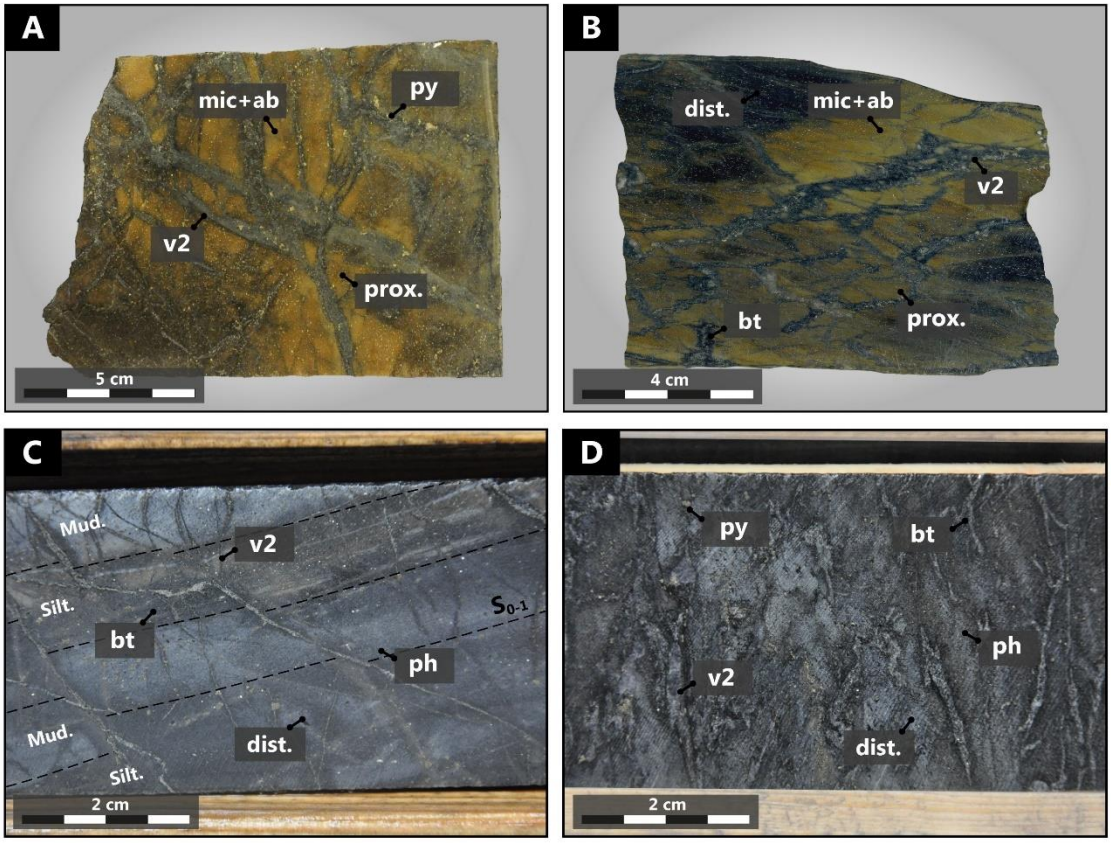

***Figure 5**: Features of the proximal and distal hydrothermal alteration in the metasedimentary rocks of the Canadian Malartic deposit. **A-B**: Proximal alteration is characterized by a beige/brown microcline±albite-quartz replacement-type assemblage, with subordinate phlogopite, carbonate (calcite±Fe-dolomite), pyrite and rutile. This facies typically occurs in the form of a pervasive alteration envelope around ore-stage (v2) veinlets. **C-D**: Distal alteration consisting of a blue/grey assemblage dominated by biotite, microcline ±albite, phengite, quartz, calcite, pyrite and rutile. The mineralogy of the distal alteration was controlled in part by variations in protolith grain size; phengite alteration is generally best-developed in fine-grained mudstone layers. Abbreviations: ab: albite; bt: biotite; mic: microcline; ph: phengite; py: pyrite; qz: quartz.*

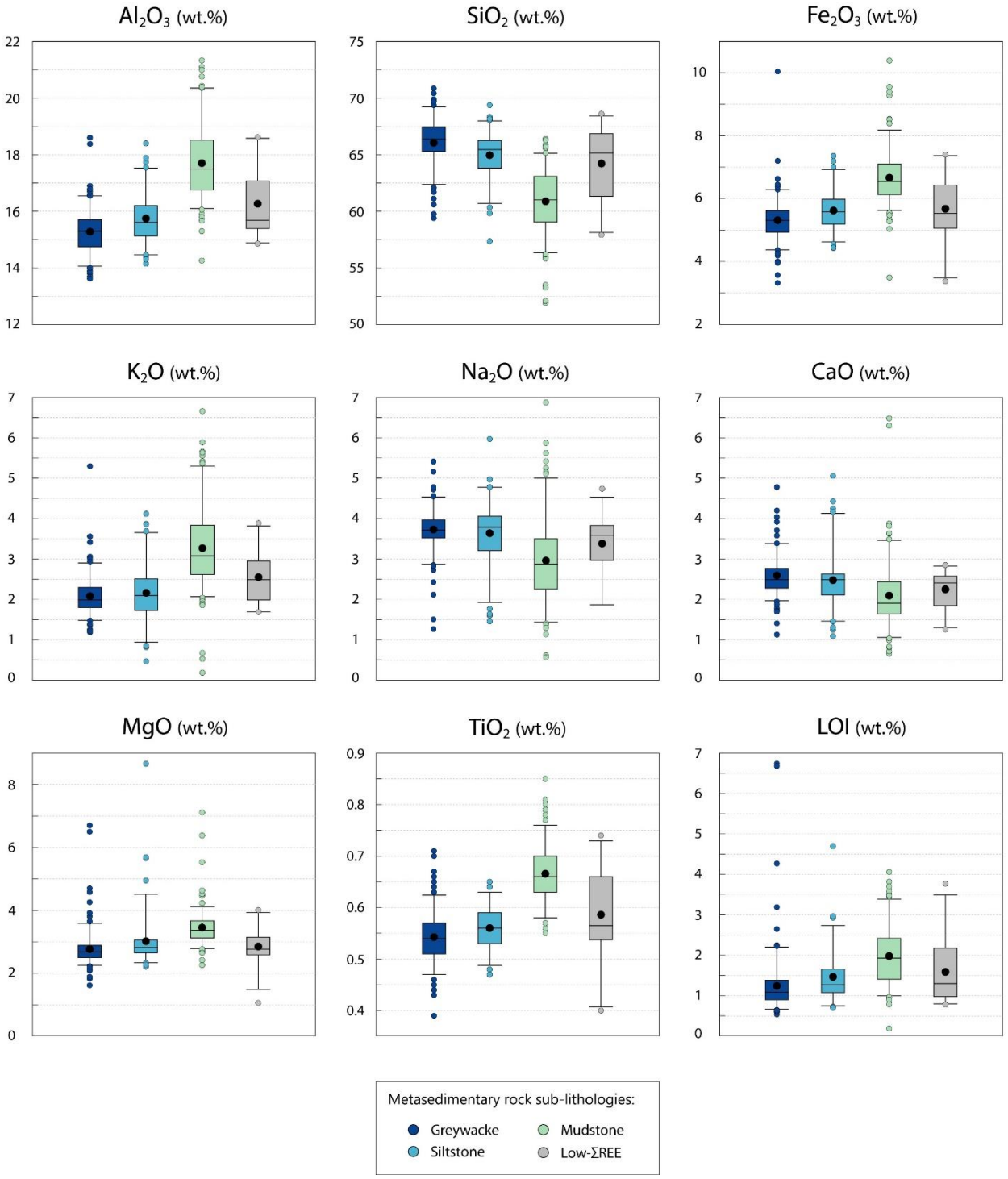

***Figure 6**: Box and whisker diagrams showing primary whole-rock lithogeochemical variations (for major elements) among the main grain size fractions of the Pontiac Group metasedimentary rocks (background population; n=443). The samples were subdivided into four lithotypes, namely greywacke (dark blue; n=171), siltstone (medium blue; n=87), mudstone (green; n=159) and low ∑REE (grey; n=26) rocks. The sediment compositions generally display clear and systematic variations with decreasing grain size.*

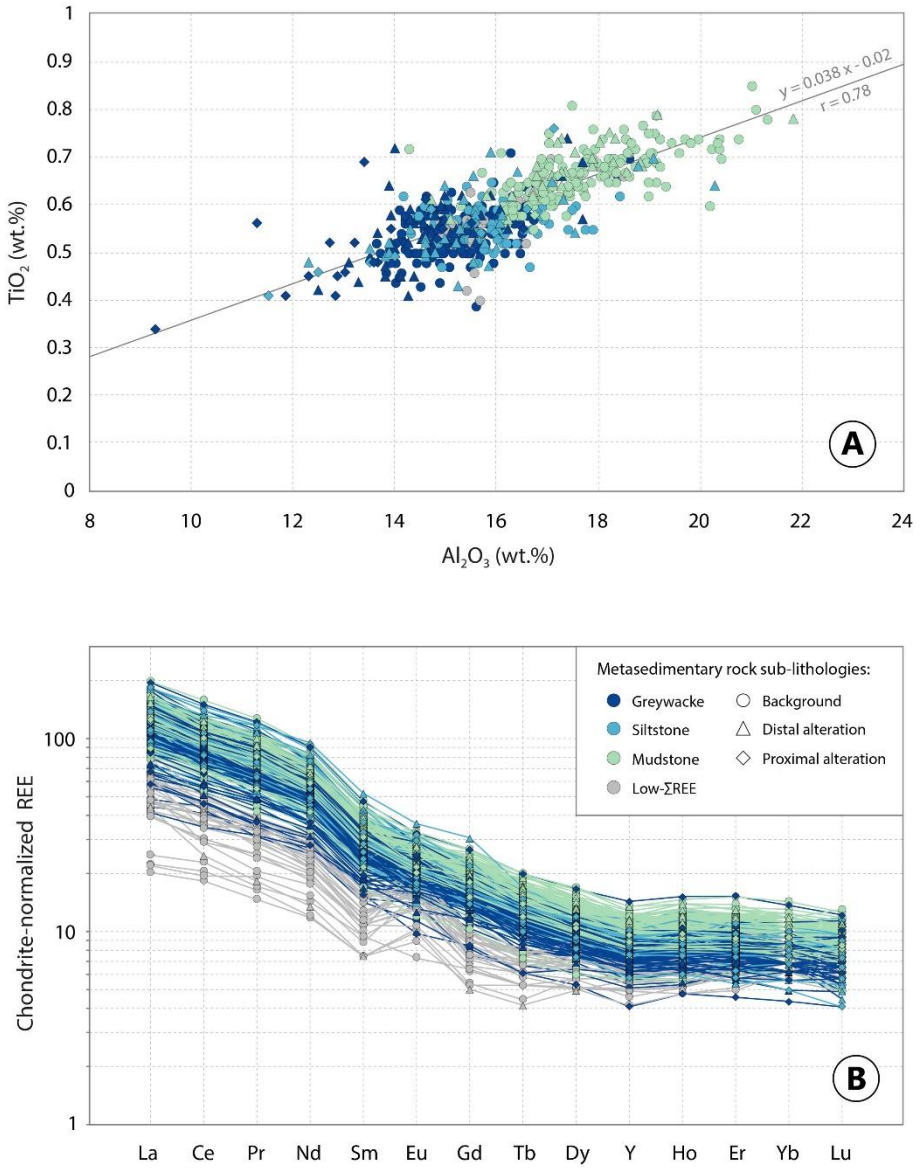

***Figure 7**: **A**: A binary plot showing a positive correlation (r=0.78) between Al_2O_3 and TiO_2 bulk-rock concentrations (in wt.%). This correlation suggests a strong cogenetic relationship for the Pontiac Group metasedimentary rock samples (n=596). The linear trend between Al_2O_3 and TiO_2 concentrations further indicates that these elements remained immobile during alteration. **B**: Chondrite-normalized REE profiles for the Pontiac Group greywacke (n=247), siltstone (n=134) and mudstone (n=188) are nearly identical and differ only in the absolute proportions of the REE. A separate group is defined by low ∑REE concentrations (n=27) and a distinct chondrite-normalized REE profile. The data for chondrite were taken from Sun and McDonough (1995).*

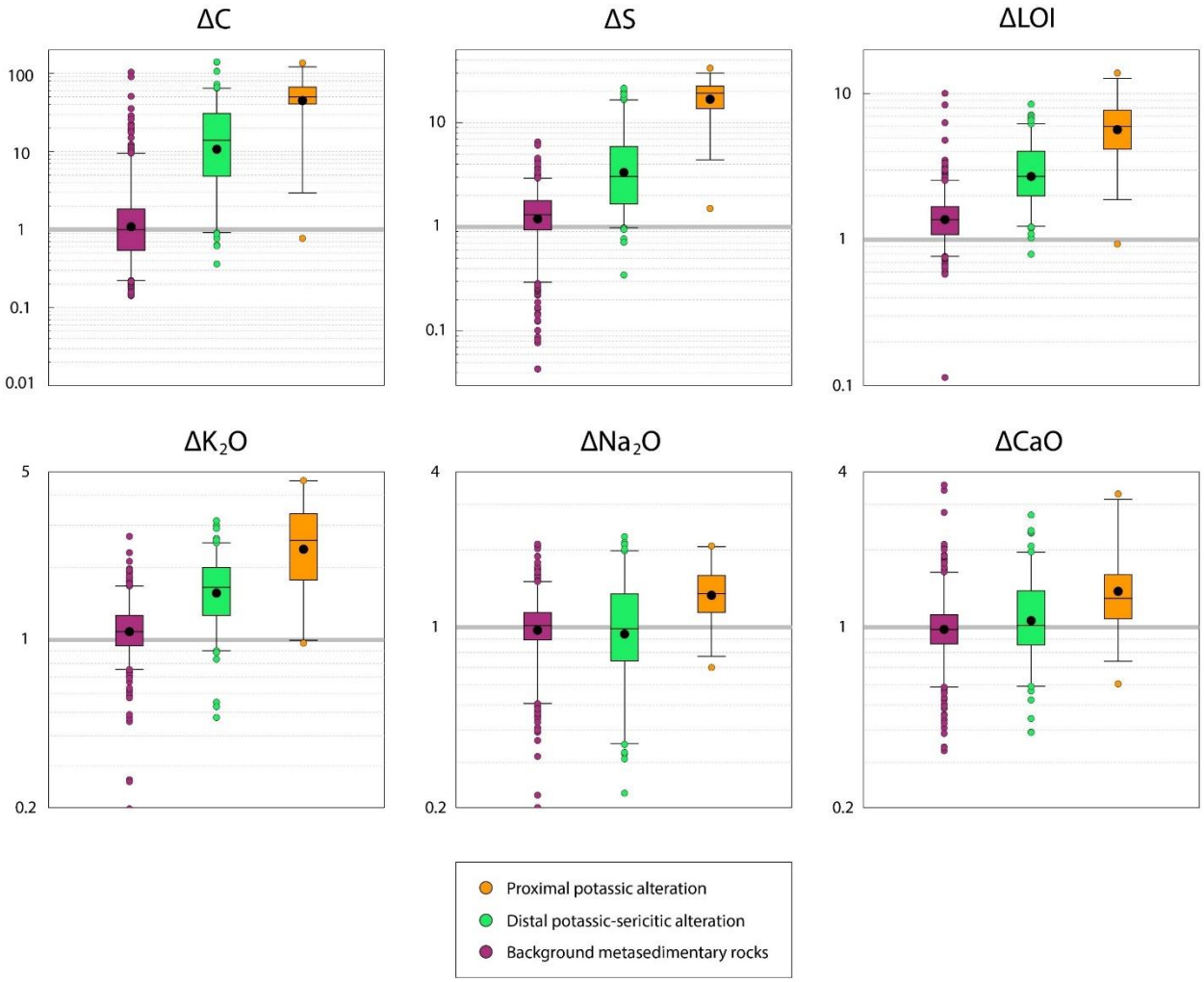

***Figure 8**: Box and whisker diagrams illustrating mass changes produced by hydrothermal alteration for selected major elements in the metasedimentary rocks of the Malartic district. The samples were divided into three groups according to alteration characteristics, from background (in purple), to distal (in green) and proximal (in orange) alteration zones.*

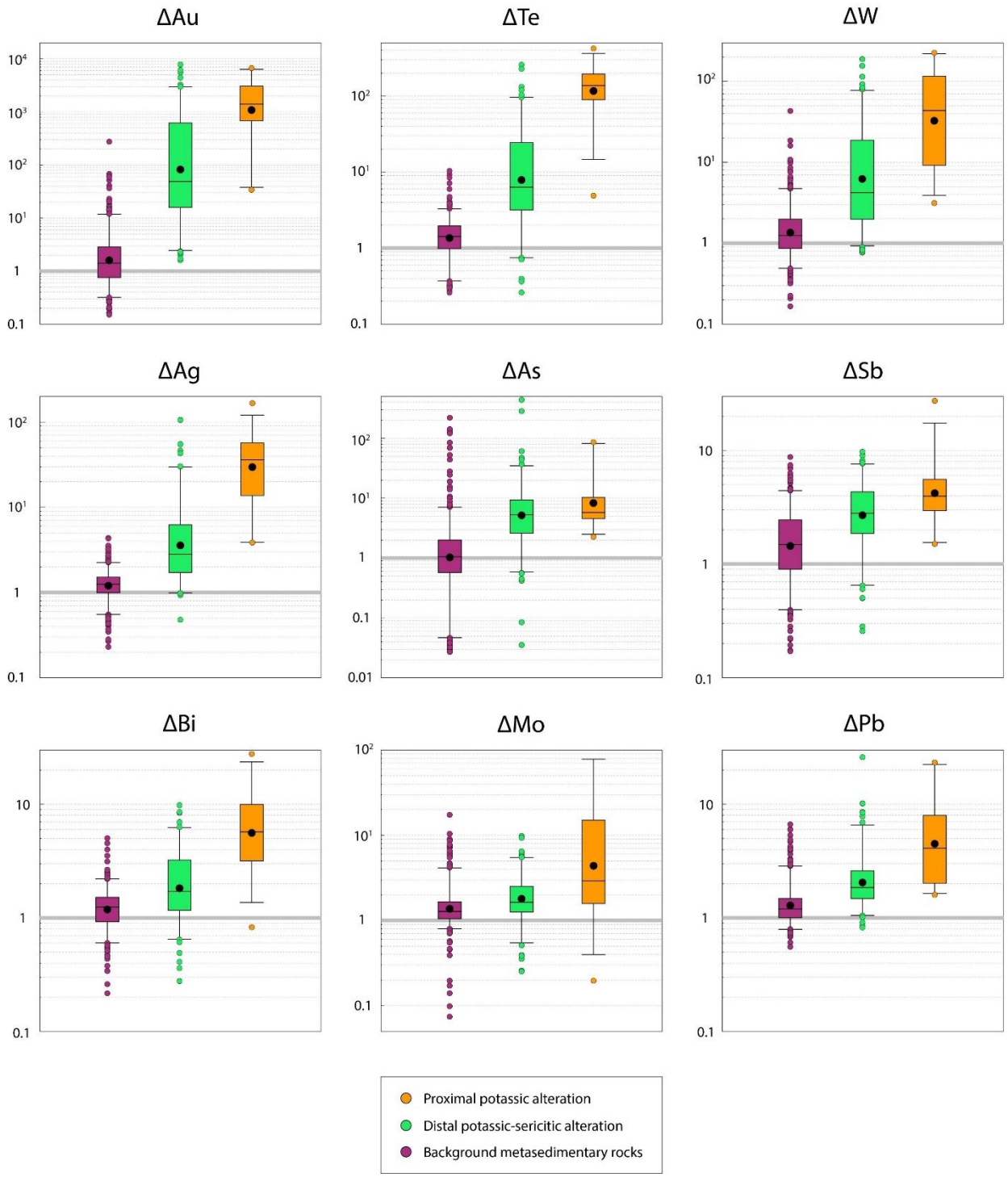

***Figure 9**: Box and whisker diagrams illustrating mass changes produced by hydrothermal alteration for selected trace elements in the metasedimentary rocks of the Malartic district. The samples were divided into three groups according to alteration characteristics, from background (in purple), to distal (in green) and proximal (in orange) alteration zones.*

	Au	K	Na	K+Na	Ca	LOI	C	S	Ag	As	Be	Bi	Cu	Mo	Pb	Sb	Se	Te	W
Au	1																		
K	0.35	1																	
Na	0.24	-0.29	1																
K+Na	0.51	**0.62**	0.54	1															
Ca	0.32	-0.02	0.41	0.28	1														
LOI	0.53	0.57	0.04	0.50	0.40	1													
C	0.51	0.49	0.19	0.56	0.51	**0.84**	1												
S	**0.66**	0.56	0.29	**0.72**	0.35	**0.75**	**0.64**	1											
Ag	**0.62**	0.45	0.19	0.55	0.28	**0.66**	0.54	**0.82**	1										
As	0.03	0.14	-0.11	0.06	0.05	0.19	0.14	0.10	0.07	1									
Be	0.58	**0.63**	0.19	**0.69**	0.31	**0.74**	**0.70**	**0.70**	0.59	0.10	1								
Bi	0.48	0.43	0.14	0.47	0.24	**0.60**	0.46	**0.72**	0.57	0.02	0.57	1							
Cu	0.06	0.02	0.01	0.02	0.17	0.10	0.02	0.17	0.19	-0.02	0.09	0.00	1						
Mo	0.22	0.28	0.09	0.31	0.19	0.40	0.29	0.41	0.37	-0.01	0.39	**0.65**	-0.14	1					
Pb	0.34	0.35	0.20	0.47	0.18	0.45	0.41	0.50	0.44	0.00	0.53	**0.64**	-0.06	0.50	1				
Sb	0.20	0.31	0.09	0.35	0.19	0.40	0.36	0.43	0.31	0.28	0.27	0.24	0.04	0.11	0.16	1			
Se	0.32	0.32	0.19	0.44	0.31	0.41	0.42	0.59	0.43	0.08	0.45	0.44	0.35	0.23	0.36	0.24	1		
Te	**0.66**	0.55	0.21	**0.65**	0.28	**0.70**	**0.60**	**0.87**	**0.94**	0.07	**0.68**	**0.64**	0.11	0.39	0.50	0.32	0.44	1	
W	**0.64**	0.38	0.28	0.56	0.28	0.53	0.49	**0.63**	0.59	0.01	0.53	0.43	0.00	0.22	0.38	0.19	0.28	**0.70**	1

***Figure 10**: A Pearson correlation matrix of the mass change values (enrichment factors) calculated for selected major and trace elements in the metasedimentary rocks of the Malartic district (n=596).*

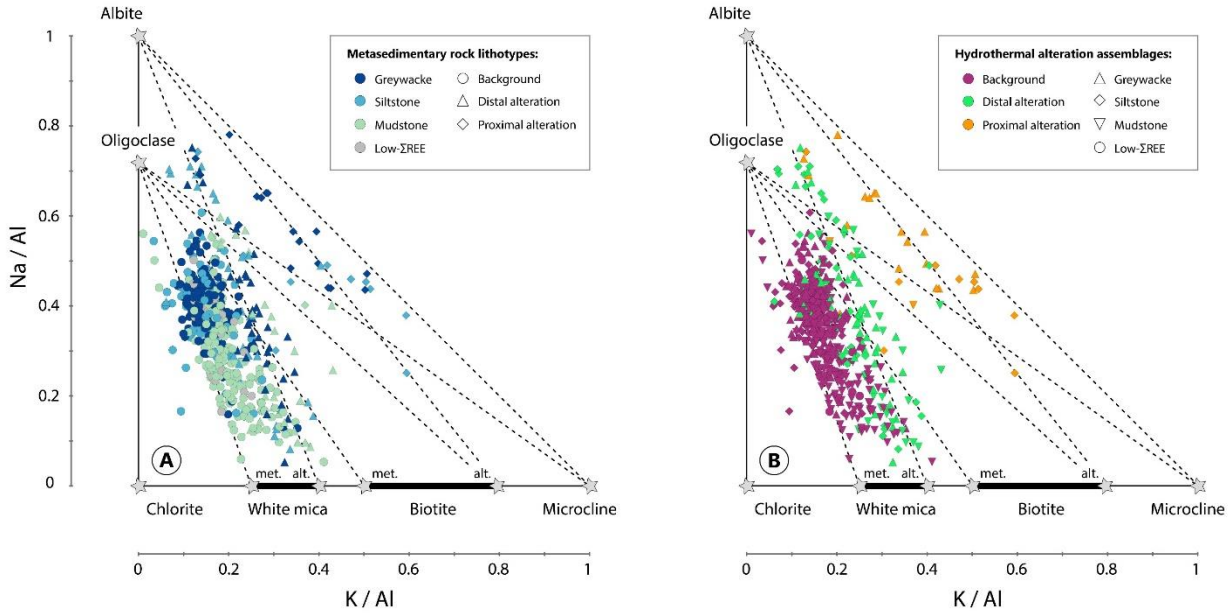

Figure 11: *Binary plots of alkali/aluminum molar ratios (Na/Al vs. K/Al) for background and altered metasedimentary rocks of the Malartic district (n=596).* ***A****: The effects of primary sedimentary processes on the whole-rock molar element ratios. The samples are grouped into four lithotypes, namely greywacke (dark blue), siltstone (medium blue), mudstone (green) and low ∑REE (grey) metasedimentary rocks.* ***B****: The effects of hydrothermal alteration on whole-rock molar element ratios. The samples are grouped into three categories based on alteration characteristics, from background (purple), to distal (green) and proximal (orange) alteration zones. The bold lines for biotite and white mica represent the range of mineral compositions determined from electron microprobe analyses (Gaillard et al., 2018). Abbreviations: alt: altered; met: metamorphic*

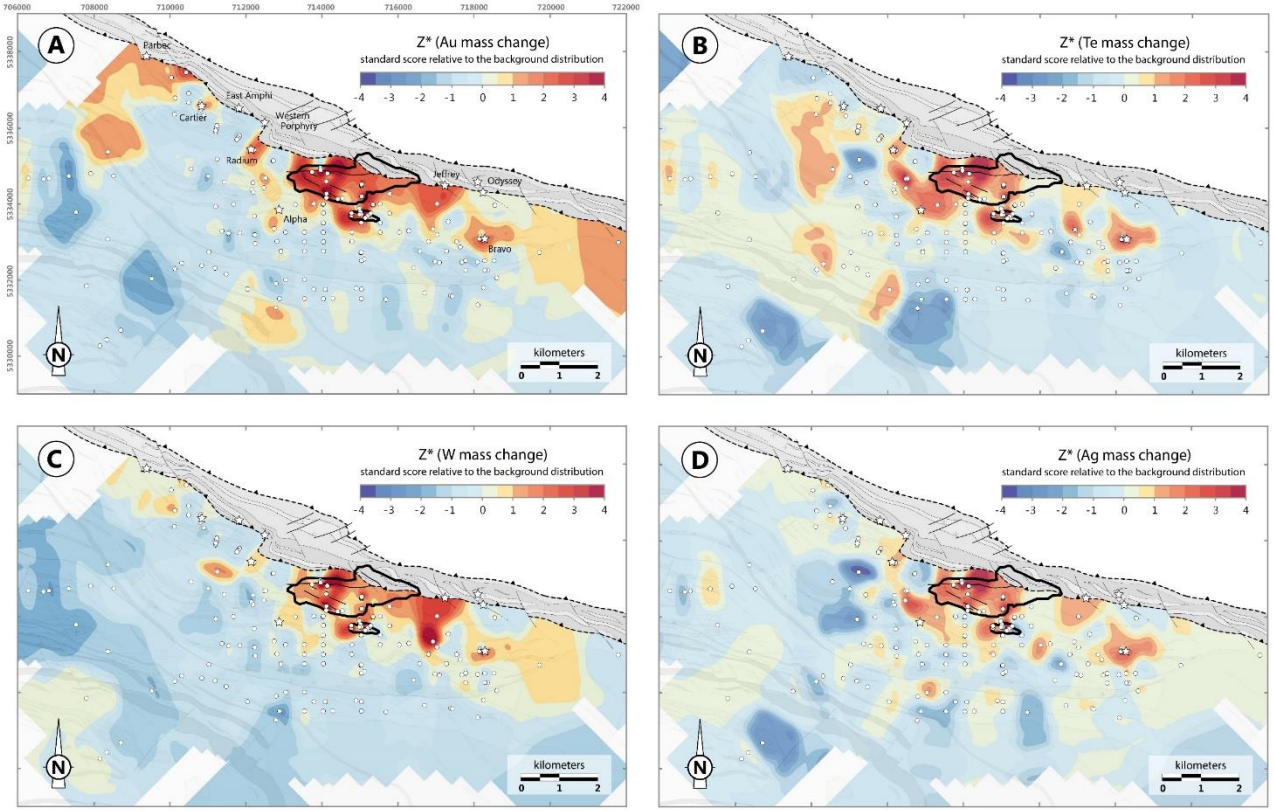

Figure 12: *A series of interpolated lithogeochemical maps illustrating mass changes associated with hydrothermal alteration in the metasedimentary rocks of the Malartic district. The mass change values for Au (A), Te (B), W (C) and Ag (D) are expressed in terms of standard deviation distance relative to the background population mean (Z*). See text for details on the calculation method. The white dots show the sample locations (n=596). The main gold occurrences outside of the Canadian Malartic deposit are represented by star symbols.*

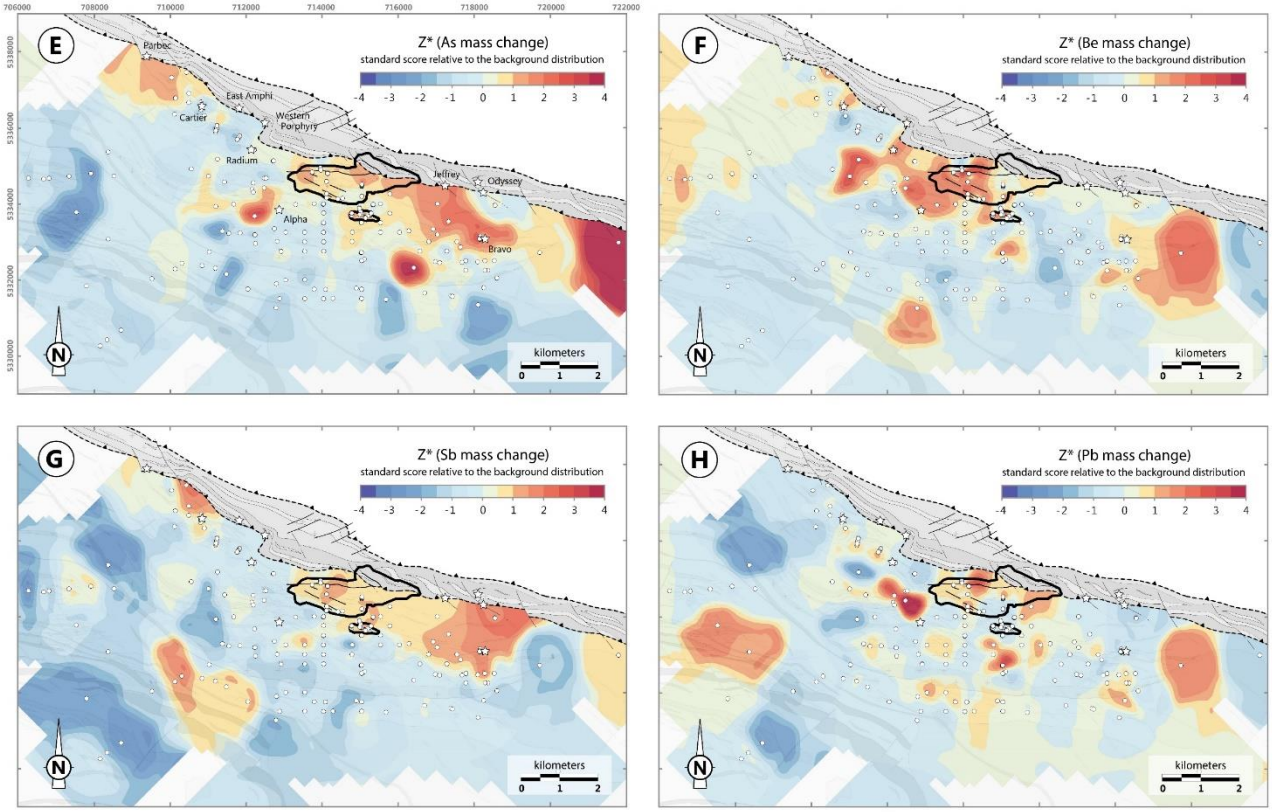

Figure 12 (continued): *A series of interpolated lithogeochemical maps illustrating mass changes associated with hydrothermal alteration in the metasedimentary rocks of the Malartic district. The mass change values for As (E), Be (F), Sb (G) and Pb (H) are expressed in terms of standard deviation distance relative to the background population mean (Z*). See the text for details on the calculation method. The white dots show the sample locations (n=596). The main gold occurrences outside of the Canadian Malartic deposit are represented by star symbols.*

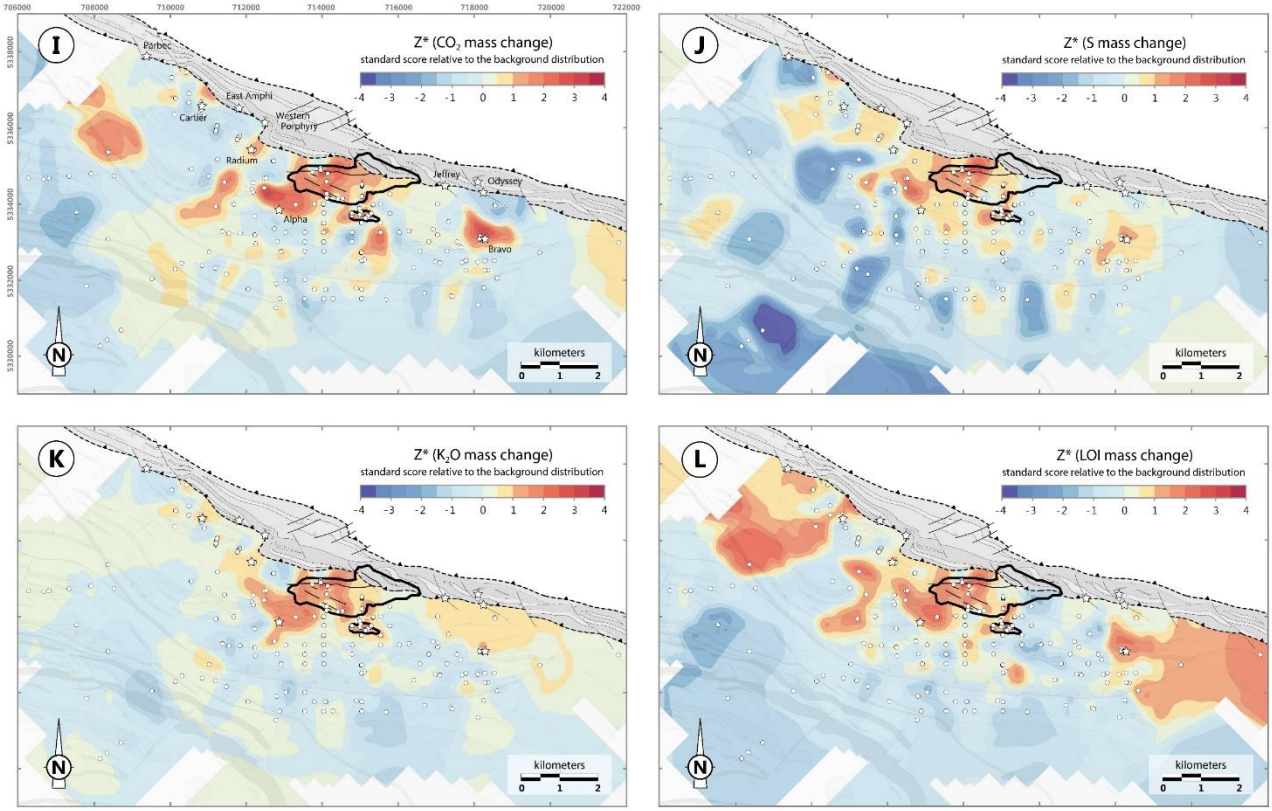

Figure 12 (continued): *A series of interpolated lithogeochemical maps illustrating mass changes associated with hydrothermal alteration in the metasedimentary rocks of the Malartic district. The mass change values for CO_2 (I), S (J), K_2O (K) and LOI (L) are expressed in terms of standard deviation distance relative to the background population mean (Z*). See the text for details on the calculation method. The white dots show the sample locations (n=596). The main gold occurrences outside of the Canadian Malartic deposit are represented by star symbols.*

APPENDICES

Appendix 1: *Whole-rock compositions of Pontiac Group metasedimentary rocks in the Canadian Malartic district (raw data).*

Appendix 2: *Mass changes calculated for major and trace elements in the metasedimentary rocks of the Malartic district (enrichment factors).*

Appendix 3: *Standardized mass change values for major and trace elements in the metasedimentary rocks of the Malartic district. Mass transfer data were transformed using a Z-score standardization algorithm ($Z^{*}_{\Delta X}$), and expressed in units of multiplicative standard deviation (s^{*}) relative to the geometric mean ($\bar{x}^{*}$) of the background metasedimentary rocks.*

Appendix 4*: Box and whisker plots showing the primary whole-rock lithogeochemical variations (for minor elements) among the main grain size fractions of the Pontiac Group metasedimentary rocks (background population; n=443). The samples were separated into four lithotypes, namely greywacke (dark blue; n=171), siltstone (medium blue; n=87), mudstone (green; n=159) and low ∑REE (grey; n=26) sediments. The bulk-rock sediment compositions display systematic variations with decreasing grain size.*

Appendix 5*: A Pearson correlation matrix of log-transformed mass change values (enrichment factors) calculated for selected major and trace elements in the metasedimentary rocks of the Malartic district (n=596).*